Detailed structural orchestration of Lewy pathology in Parkinson's disease as revealed by 3D multicolor STED microscopy

Tim E. Moors[1], Christina A. Maat[1], Daniel Niedieker[2], Daniel Mona[3], Dennis Petersen[2], Evelien Timmermans-Huisman [1], Jeroen Kole[4], Samir F. El-Mashtoly[2], Wagner Zago[5], Robin Barbour[5], Olaf Mundigl[6] , Klaus Kaluza[6], Sylwia Huber[7], Melanie N. Hug[7], Thomas Kremer[3], Mirko Ritter[8], Sebastian Dziadek[9], Jeroen J.G. Geurts[1], Klaus Gerwert[2], Markus Britschgi[3], Wilma D.J. van de Berg[1]*

[1]Amsterdam UMC, Vrije Universiteit Amsterdam , Department of Anatomy and Neurosciences, Section Clinical Neuroanatomy, Amsterdam Neuroscience, De Boelelaan 1117, Amsterdam, The Netherlands.

[2]Department of Biophysics, Ruhr-University Bochum, Bochum, Germany

[3] Roche Pharma Research and Early Development; Neuroscience, Ophthalmology, and Rare Diseases Discovery and Translational Area, Roche Innovation Center Basel, Switzerland

[4] VU University Medical Center, Department of Physiology, Amsterdam, The Netherlands.

[5] Prothena Biosciences Inc, South San Francisco, California, USA

[6] Roche Pharma Research and Early Development; Therapeutic Modalities; Large Molecule Research, Roche Innovation Center Munich, Germany

[7] Roche Pharma Research and Early Development; Therapeutic Modalities; Small Molecule Research, Roche Innovation Center Basel, Switzerland

[8] Roche Diagnostics GmbH, Penzberg, Germany

[9] Roche Pharma Research and Early Development; Oncology Discovery and Translational Area, Roche Innovation Center Basel, Switzerland

***Corresponding author:**

Wilma D.J. van de Berg, PhD

Dept. of Anatomy & Neurosciences, chair section Clinical Neuroanatomy and Biobanking

Amsterdam Neuroscience

Amsterdam UMC, location VU University Medical Center

O2 building, room 13 E11

De Boelelaan 1108

1081 HZ Amsterdam, the Netherlands

e-mail: wdj.vandeberg@vumc.nl; Tel.nr: +316-25694907

Abstract

Post-translational modifications of alpha-synuclein (aSyn), in particular phosphorylation at Serine 129 (Ser129-p) and truncation of its C-terminus (CTT), have been implicated in Parkinson's disease (PD) pathophysiology. Although great interest has emerged for these species as potential biomarkers and therapeutic targets in PD, little is known about their (sub)cellular manifestation in the human brain. In this study, we mapped distribution patterns of Ser129-p and CTT aSyn in neurons with and without Lewy pathology. The combination of highly selective antibodies with multicolor STED microscopy allowed detailed phenotyping of subcellular neuropathology in PD. Nigral Lewy Bodies revealed an onion skin-like 3D architecture, with a framework of Ser129-p aSyn and neurofilaments encapsulating CTT and membrane-associated aSyn epitopes. Based on the identification of subcellular pathological phenotypes in this study we present a novel hypothesis for maturation stages of Lewy pathology and provide evidence for a key role for Ser129-p aSyn in Lewy inclusion formation.

Introduction

The presence of cellular inclusions – termed Lewy Bodies (LBs) and Lewy Neurites (LNs) – in predilected brain regions pathologically defines Parkinson's disease (PD) and dementia with Lewy bodies (DLB). LBs and LNs are defined as eosinophilic inclusions with different morphologies, typically dependent on brain region (brainstem, limbic or cortical) [1, 2]. To this end, the mechanism determining the formation and morphology of these inclusions remains elusive. LBs and LNs are strongly immunoreactive for alpha-synuclein (aSyn), which is one of their major components [3]. aSyn is a 14kDa protein ubiquitously and highly expressed in neurons under physiological conditions. Its enrichment in presynaptic terminals has been established [4-7], while more recent studies have reported additional intraneuronal localizations for aSyn, including mitochondria, endoplasmatic reticulum (ER) and Golgi [7]. The primary sequence of aSyn contains 140 amino acids, and is composed of three distinct domains. An important role has been proposed for the lipophilic N-terminus (NT) and non-amyloid component domain (NAC domain) in the interaction of aSyn with membranes as the first 93 residues can adopt an alpha-helical conformation in the presence of lipids, and they bear the locations for the currently known point mutations in aSyn that lead to familial forms of PD [7, 8]. Residues 96-140 encompass the negatively charged, acidic C-terminus (CT) of aSyn for which important roles have been proposed in the interaction of aSyn with other proteins or metal ions [9]. The CT further harbors the majority of sites where aSyn can be post-translationally modified (PTM) [10].

The list of aSyn PTMs detected in the human brain has grown extensively in recent years, which highlights the physicochemical and structural flexibility of aSyn [11, 12]. Some of these PTMs have been implicated in PD pathology - in particular the phosphorylation at Serine 129 (Ser129-p) and truncations of the C-terminus (CTT). Ser129-p aSyn and different CTT fragments of aSyn, with cleavage sites for instance at residues 119 (119CTT) and 122

(122CTT), were identified in pathology-associated fractions of the DLB brain using mass spectrometry and immuno-based biochemical assays [13, 14]. Immunohistochemical analyses in postmortem brain tissue of DLB patients and also aSyn transgenic mouse brains point to a potential role of 122CTT in axonal and synaptic degeneration [15]. Although Ser129-p and CTTaSyn can be detected in small amounts under physiological circumstances [16], these PTMs are enriched under pathological conditions [13, 14, 17-19]. Experimental studies have suggested an important role for CTT in aSyn aggregation, as enhanced fibril formation was reported for this PTM with recombinant aSyn *in vitro* [19-23]. However, the exact role of CT modification by either phosphorylation or truncation in aSyn aggregation and toxicity, remains subject of active debate [24].

A great interest has emerged for PTM aSyn as a potential biomarker and therapeutic target for PD [25, 26], and led to the development of new research tools, including antibodies specifically directed against Ser129-p and CTT aSyn. Although such antibodies were reported to show immunoreactivity in LBs and LNs [13, 14, 27], only little is known about their detailed immunoreactivity patterns in the human brain under physiological and pathological conditions. More information on their subcellular distribution is crucial for a better understanding of the physiological and pathological relevance of Ser129-p and CTT aSyn, and therefore highly relevant for ongoing and upcoming immunovaccination therapies targeting different aSyn species.

In this study, we aimed to define spatial distribution and (sub)cellular manifestation of Ser129-p and CTT aSyn in human brain tissue with and without Lewy pathology. For this purpose, we mapped immunoreactivity patterns of highly selective antibodies directed against Ser129-p and CTT aSyn in postmortem brain tissue of PD patients and non-neurological subjects using high-resolution 3D confocal scanning laser microscopy (CSLM) and stimulated emission depletion (STED) microscopy. Our results provide novel insights into antibody-

labeled subcellular pathology in PD, demonstrating a systematic onion-like architecture of nigral LBs with differential affinities for different aSyn epitopes. Ser129-p aSyn at the periphery of these onion-skin type LBs was associated with a cage-like framework of intermediate neurofilaments. Label-free coherent anti-Stokes Raman scattering microscopy revealed the presence of increased lipid and protein contents in the center of a-Syn immunopositive inclusions, suggesting encapsulation of these components in the core of LBs. Cytoplasmic CTT reactivity was associated with mitochondria, while Ser129-p aSyn was structured in a filamentous network in diseased neurons in the PD brain, possibly representing an early stage of Lewy inclusion formation. Based on the identification of subcellular pathological phenotypes in this study, we present an hypothesis for maturation stages of Lewy pathology and provide evidence for a key role for Ser129-p aSyn aSyn in Lewy inclusion formation.

Results

Morphological features of aSyn-positive inclusions as labeled by antibodies against different epitopes

In accordance with existing literature [13, 14, 27], immunohistochemical (IHC) stainings using antibodies (specified in Table S1) against truncated aSyn species (119 and 122 CTT aSyn) and Ser129-p aSyn labeled pathology-associated morphologies in post-mortem brain tissue from clinically diagnosed and neuropathologically confirmed advanced PD patients (Braak 5/6; Table S2), including LBs and LNs. These neuronal inclusions were also detected using antibodies directed against epitopes within specific domains (CT, NT and NAC domain), while this group of antibodies also revealed synaptic-like staining profiles, particularly in the hippocampus and transentorhinal cortex. Representative images of neuronal aSyn-positive inclusions labeled with antibodies against different epitopes, taken in the

substantia nigra (SN), hippocampus and transentorhinal cortex of PD patients, are shown in Figure S1, together with KM-51, an antibody commonly used for neuropathological diagnosis [28].

We defined two main types of intracytoplasmic aSyn-immunopositive inclusion bodies based on the observed IHC labeling profiles. Many of the spherical LBs in the SN displayed immunoreactivity in targetoid appearance, i.e. with a strong immunopositive ring surrounding a central – weakly or unstained - core (Fig. S1A). Inspection in adjacent brain sections of the same patients suggested that this morphological appearance of LBs was most clearly visualized by antibodies against Ser129-p aSyn and CT aSyn (Fig. S1A, xiv, xxvi). Antibodies directed against other aSyn epitopes generally revealed less contrast between core and immunoreactive ring. In some LBs, an area of weaker immunoreactivity surrounding the strongest immunopositive portion of the LB could also be observed (f.i. Fig. S1A, xviii). The targetoid appearance of LBs has been described with many antibodies against aSyn in literature, and a subset of these morphologies were shown to represent the eosinophilic 'classical LBs' unambiguously identified by hematoxylin and eosin stainings [2]. Peripheral immunoreactivity surrounding a weakly stained central core could also be observed in a subset of the dystrophic LNs in the SN (Fig. S1B).

Other intracytoplasmic aSyn positive inclusions showed diffuse and uniform labeling throughout the structure. This IHC pattern was generally observed for limbic and cortical LBs in the hippocampal CA2 region and transentorhinal cortex, respectively, but also for certain inclusions in the SN [1, 2]. The shapes of this latter group of inclusion bodies showed substantial heterogeneity, including both globular structures (f.i. Fig. S1A, xxiii), as well as irregularly-shaped expansive-appearing cytoplasmic inclusions (f.i. Fig. S1A, i&iii).

Onion skin-like distribution of aSyn epitopes in Lewy inclusions

Triple labeling immunofluorescence experiments demonstrated that Ser129-p aSyn, 119CTT and 122CTT only partially co-localized in nigral LBs, using different combinations of antibodies (Table S2). In particular, Ser129-p immunopositive rings in nigral LBs localized consistently more towards their periphery as compared to staining patterns for 119CTT or 122CTT aSyn (Fig. 1A, C, Video S1,2). Interestingly, different localization patterns were also observed between antibodies against NAC, NT and CT of aSyn, with CT aSyn immunoreactivity surrounding the other domains (Fig. 1B, D, Video S3). A combination of these antibodies in different multiple labeling protocols revealed a gradual distribution of immunoreactivities in nigral LBs (Fig. 2A). This lamellar organization of different concentric rings together revealed an onion skin-like 3D morphology of LBs (Fig 2E, Video S4), with pronounced reactivity for CT and Ser129-p aSyn at the periphery, while antibodies against CTT aSyn, NT and NAC aSyn localized more towards the core of these structures (Fig. 2A-C). The same build-up was observed using a set of different antibodies directed against similar epitopes (Fig. S2). The consistency of this observation was semi-quantitatively examined in 29 LBs in SN sections of 8 PD patients. For each LB, relative signal intensities (as % of peak intensity) were plotted per channel over a normalized LB diameter. The resulting average line profile revealed a clear separation of peak intensity localizations for the different aSyn epitopes, revealing that this gradual distribution was consistent ($p < 0.0001$; Fig. 2F; Table S3), while 3D CSLM analyses further showed that the lamellar build-up was present throughout the entire structure (Fig. 2E, Video S4). Converging DAPI reactivity was consistently observed at the core of these inclusions, although this signal was generally weaker than its staining intensity in neighboring cell nuclei (Fig. 2B). Numerous dystrophic LNs in the SN were observed to contain compositions similar to these LBs (Fig. 2D).

Distribution patterns for different aSyn epitopes were also analyzed in Ser129-p positive inclusion bodies in which no ring-like appearance was observed, in the same sections

(in case of SN) and in other sections of the same patients (hippocampus/transentorhinal cortex). These inclusion bodies were homogeneously labeled for Ser129-p aSyn, except for typical 'cavities' lacking Ser129-p reactivity (Fig. S3A,D). Although such inclusions were unambiguously stained for Ser129-p aSyn, antibodies against other aSyn epitopes (particularly 122CTT, NAC and NT aSyn) generally revealed weak signal intensities that were distributed diffusely throughout the inclusion, while immunoreactivity for DAPI was barely increased compared to the surrounding. Although these inclusions appeared relatively unstructured – e.g. no systematic distribution patterns for aSyn epitopes were observed - their outline was usually sharply demarcated by Ser129-p aSyn immunoreactivity (f.i. Fig. S3A, Video S5). Taken together, our results show morphology-dependent distribution patterns for aSyn epitopes in Ser129-p aSyn-positive inclusions, and provide evidence for a structured lamellar and onion skin-like 3D organization of certain midbrain LBs and LNs.

Centralization of lipids and proteins in nigral LBs

As we observed different localization for antibodies recognizing membrane-associated aSyn domains (NT/NAC domain) and CT recognizing antibodies, we explored whether this differential epitope availability could be explained by the distribution patterns of proteins and lipids in LBs. For this purpose, we used a label-free optical imaging technique, CARS microscopy, in combination with CSLM. In total, 57 Ser129-p aSyn-positive inclusions were scanned in SN sections of 5 PD patients (Table S1). Results revealed substantial heterogeneity in protein and lipid distributions in the Ser129-p immunopositive inclusions, both within and between patients (Fig. 3D). We identified inclusions with different chemical compositions: part of the inclusion bodies showed high protein and lipid content as compared to the direct environment (35%), others contained higher protein content but no increased lipid content (30%), and finally inclusions were observed without detectable increases for either lipid or protein content (35%) (Fig. 3A-C). In 14 out of 20 inclusions with increased lipid content,

lipids clustered at their central portion, while a similar pattern was observed for proteins (28 out of 37 inclusions). In all inclusions with centralized lipids, an increased protein content was also detected in the core (14 out of 14 inclusions). Overall, our results show that in the subset of aSyn-positive inclusion bodies that shows increased protein and lipid content compared to the surrounding, these components are generally found centralized in the structure, suggesting an encapsulation of highly aggregated material in LBs.

Ser129-p aSyn and cytoskeletal proteins form filamentous cage at the periphery of LBs

The previously described results together suggest a structured, lamellar architecture of LBs. As cytoskeletal proteins are a major constituent in organizing cellular organelles and substructures, we therefore explored the distribution of intermediate neurofilaments and beta-tubulin in the described onion-skin type LBs, and their association with Ser129-p aSyn immunoreactivity patterns. Although LBs are defined in brightfield microscopy as spherical smooth-edged inclusions, detailed STED imaging revealed that the outline of many LBs revealed a corona of radiating immunoreactivity, best – but not exclusively - visualized using antibodies against Ser129-p aSyn (Fig. S4). The radiating Ser129-p immunoreactivity patterns resembled the shape and orientation of filaments (Fig. S4, Fig. 4) described in early electron microscopy (EM) studies of LBs [29, 30].

Co-staining of Ser129-p aSyn with markers for intermediate neurofilament and beta-tubulin showed immunoreactivity for cytoskeletal markers at the periphery of nigral LBs (Fig. 4). Together with Ser129-p aSyn, these markers visualized a filamentous ‘cage-like’ framework (Fig. 4D). Beta-tubulin reactivity was also present at the periphery of LBs, where it overlapped substantially with Ser129-p aSyn. Moreover, beta-tubulin also revealed filamentous structures with radiating orientation, although even more localized towards the periphery of the LB (Fig. 4B). Neurofilament reactivity showed a different distribution, as it

visualized two rings: one ring localized at the central portion of the Ser129-p aSyn immunopositive band in LBs, while another ring surrounded the Ser129-p/beta tubulin signals. Interestingly, these rings were connected by radiating filamentous structures, giving rise to a structure resembling a wheel (Fig. 4D). The structure of this filamentous framework and its positioning around the Ser129-p immunopositive band could be best observed in 3D reconstructions (Video S6).

Interestingly, in other cytoplasmic inclusion morphologies or in dystrophic LNs, this arrangement of cytoskeletal components was not observed, although weak and diffuse immunoreactivity of cytoskeletal markers was generally present. This suggests that the organization of Ser129-p aSyn and cytoskeletal markers was typical for cytoplasmic inclusions, in particular for the before-mentioned 'onion skin-type' LBs (Fig. S5 A,C).

Different subcellular manifestations for Ser129-p and CTT aSyn

Apart from their localization in aSyn-immunopositive inclusion bodies, Ser129-p and 122CTT aSyn antibodies also revealed cytoplasmic immunoreactivity in neurons outside of these structures. Immunoreactivity for 119CTT was specific for pathological inclusions with limited immunoreactivity in the cytoplasm. The appearance of cytoplasmic reactivity was different for Ser129-p and 122CTT aSyn (Fig. 5A). In particular, 122CTT aSyn revealed many immunoreactive punctae throughout the neuronal cytoplasm, while Ser129-p aSyn immunoreactivity visualized an intracytoplasmic network of thin fibers. Limited co-localization was observed between these signals (Fig 5A).

122CTT aSyn immunopositive punctae are associated with mitochondria

122CTT immunopositive punctae were not only observed in PD patients, but also in brain tissue sections of donors without Lewy pathology (Fig. S6A). The pattern appeared more pronounced in the hippocampus and transentorhinal cortex compared to the SN (Fig.

5B). We observed the punctate reactivity pattern of 122CTT aSyn using different antibodies against this epitope (syn105 and asyn-134), while this pattern was not observed for 119CTT aSyn. These 122CTT aSyn-reactive punctae were more pronounced in the cytoplasm of neurons compared to the environment. Analysis with subcellular markers revealed that a subset of the 122CTT-reactive punctae in the cytoplasm of neurons co-localized with mitochondrial morphologies immunoreactive for Porin/VDAC reactivity, which is a marker for the outer membrane of mitochondria (Fig. 5B). This association between CTT aSyn and mitochondria was also observed in 3D (Video S7). Together, our findings suggest widespread 122CTT aSyn expression in the brain of donors with and without PD, particularly in the neuronal cytoplasm where 122CTT aSyn is possibly associated with mitochondria.

Antibodies against Ser129-p aSyn reveal intracytoplasmic network

The Ser129-p aSyn immunopositive fibrous network was frequently visible in large neuromelanin-containing neurons in the SN (Fig. 5C). Most often, the network was observed in many neurons containing an expansive-appearing inclusion uniformly stained for Ser129-p aSyn, and in a smaller fraction of neurons containing onion-skin type LBs. However, this network was also observed in a subset of neuromelanin-containing neurons without apparent inclusion in PD patients (f.i. Fig. 6A, 1). Other neurons without inclusion in donors with PD did not reveal a Ser129-p aSyn immunopositive network, while it was not observed in donors without Lewy pathology (Figure S6B). The Ser129-p aSyn reactive fibers did not co-localize with markers for intermediate neurofilaments, beta-tubulin (Fig. 5C) or endoplasmatic reticulum (ER; Fig. S5), indicating that the alignment of Ser129-p positive fibers is not explained by localization of Ser129-p aSyn to these intracytoplasmic networks. The observed diameter of the structures in the network was generally 70-80 nm and limited by the resolution of the applied scan settings of the STED microscope. Together, these observations

suggest that the Ser129-p aSyn immunopositive filamentous network is a pathological feature, possibly representing an early stage of Lewy pathology.

Intraneuronal reactivity patterns of Ser129-p aSyn allows identification of pathological subcellular phenotypes

By comparing cytoplasmic Ser129-p aSyn-immunoreactivity patterns with different specific antibodies within and between patients, we were able to identify several commonly observed reactivity patterns in melanin-containing neurons of brains with Lewy pathology. Representative examples for these subcellular pathological phenotypes are summarized in Fig. 6A, as visualized by CSLM 3D reconstructions of large z-stacks of neuromelanin-containing nigral neurons in adjacent brain sections of the same patient. Commonly observed cellular phenotypes in the SN of PD patients based on Ser129-p aSyn immunoreactivity included: 1) neurons with Ser129-p aSyn immunopositive cytoplasmic network but without apparent inclusion; 2/3) neurons with network and smaller inclusions with uniform Ser129-p aSyn labeling; 4) neurons revealing a Ser129-p aSyn immunopositive network and (a combination of) and uniformly stained and onion skin-like inclusions; 5) neurons with a Ser129-p aSyn immunopositive network and onion skin-type inclusions – often containing radiating filaments; 6) neurons without a network, but with onion skin-type inclusion. These different faces of Ser129-p aSyn immunoreactivity possibly reflect different stages of LB formation (Figure 6B, as discussed later in the text), and may suggest a role for Ser129-p aSyn at different stages of Lewy inclusion formation.

Discussion

aSyn has been established as a major component of Lewy pathology, but the subcellular distribution of specific pathology-associated forms of this protein – both within and outside the inclusions - is unclear. Detailed insight into the aSyn-based architecture of

neuronal inclusions may allow for a better understaining of Lewy inclusion formation, which is a key event in PD pathophysiology. In the present study we explored the subcellular distribution patterns for CTT and Ser129-p forms of aSyn by means of specific antibody multiple labeling immunostainings in brain sections of PD patients in combination with high-resolution 3D CSLM and STED microscopy. This allowed an unprecedented detailed view on antibody-labeled subcellular pathological phenotypes, revealing several novel aspects of Lewy pathology.

First, we observed a Ser129-p-immunopositive cytoplasmic network in PD patients, using different antibodies directed against this epitope. Diffuse or granular cytoplasmic immunoreactivity has been described as a specific feature of certain antibodies against aSyn in different studies using light microscopy [2, 28], including antibodies with a proposed preferential affinity for disease-associated aSyn [31, 32]. However, to the best of our knowledge this study is the first to visualize the alignment of filamentous Ser129-p immunopositive structures in an intracytoplasmic network. This network was most often observed in the vicinity of an inclusion, although 3D revealed that this network could also be observed in neurons without apparent inclusions, indicating that this feature could represent an early phenotype of LB formation. Interesting in this perspective are the results of a previous study, which found that increased expression levels for Ser129-p aSyn in soluble fractions of cingulate and temporal cortices – as measured by western blotting – preceded the presence of histologically identified Lewy inclusions [33]. These findings suggest a role of Ser129-p aSyn already at early stages of LB formation - thereby contradicting theories that Ser129-p aSyn occurs after LB formation [24] - which may have important implications for the interpretation of results of biomarker studies measuring Ser129-p aSyn in body fluids or peripheral tissues. The notion of a role of Ser129-p aSyn early in inclusion formation is supported by the experimental findings that inclusion formation after administration of recombinant (full-

length and CTT) aSyn pre-formed fibrils is induced by recruitment of soluble endogenous aSyn and its intracellular phosphorylation at Ser129 [34]. Possible roles of Ser129-p at this stage could be a stabilizing effect on aggregating proteins [35] - Ser129-p was demonstrated to inhibit aSyn fibrillogenesis *in vitro* [24, 36] - while Ser129-p aSyn has also been suggested to serve as an activator of autophagic instruments [37, 38].

Although the different localization of the Syn105 and 11A5 antibodies in LBs and dystrophic LNs, directed against 122CTT and Ser129-p aSyn, respectively, has been described before [27], we now confirm this finding using different antibodies against similar epitopes, and for different CTT aSyn (calpain-cleaved at res. 119 and 122) species. We further observed a separation between antibodies against membrane-associated aSyn domains (NT/NAC domains) of aSyn and antibodies recognizing its CT in LBs. Integrating antibodies against these aSyn PTMs and domains in multiple labeling protocols showed a 3D onion skin-like orchestration of LBs, with concentric lamellar bands with preferential affinities for different aSyn antibodies. The consistency of this lamination was revealed by semi-quantitative analysis in a series of LBs and different PD patients. A multilamellar appearance of LBs has been described in different studies that focused on the ultrastructure of LBs using EM techniques [29, 30], while lamination patterns in LBs and dystrophic LNs were also suggested in studies using light microscopy [27, 39, 40]. Interestingly, in the present study this lamellar phenotype was visualized by the gradual distribution of immunoreactivities for antibodies directed against different epitopes on one single protein, aSyn.

As we observed clustering of membrane-associated aSyn epitopes mainly at the core of onion skin-like LBs, we explored the distribution of proteins and lipids in LBs using CARS microscopy, a label-free imaging technique. Results showed that increased lipid content could be detected in a fraction of nigral Ser129-p positive inclusions. Unfortunately, due to the limited morphology of the fresh-frozen tissue sections after CARS imaging, a

subclassification of LB morphologies by high-resolution CSLM imaging was not possible. However, in the majority of lipid-enriched inclusions, lipids were found to be centralized in the core of this structure together with proteins. In a previous study, we demonstrated the presence of lipid and membraneous structures in LBs using correlative light and electron microscopy (CLEM) and TEM, which was confirmed by CARS and Fourier transform infrared spectroscopy (FTIR) [41]. Moreover, reactivity in the core of LBs has further been described for different lipophilic dyes [40-42]. The functional relevance behind clustering of lipids in the center of LBs is not clear at this point. However, extensive experimental evidence has demonstrated the binding of aSyn to (bio)membranes, while the presence of lipid molecules was repeatedly reported to increase the aggregation rate of aSyn [43].

At the periphery of nigral onion skin-type LBs, radiating Ser129-p aSyn- and beta-tubulin-immunopositive filamentous structures could be observed, embedded in a cage-like framework of neurofilaments. The combination of CARS data and structural observations together raise the suggestion that aggregated proteins are encapsulated in the core of LBs by an organized framework of Ser129-p aSyn and cytoskeletal components. The displacement of intermediate filament proteins from their normal cellular distribution and the encapsulation of aggregated proteins by neurofilaments have been described as consistent features of intracellular aggresome formation [44, 45]. Although the arrangement of cytoskeletal structures at the periphery of LBs has been reported before, this study provides important new detailed insights into the structure of and relation between different filamentous components in LBs. Thereby, our results support previous studies proposing that LBs share phenotypic features with aggresomes [46]. Our observations indicate that the interplay of Ser129-p aSyn with cytoskeletal proteins may be an important step in the process of LB formation.

Among many features of Ser129-p Syn immunoreactivity patterns within and between PD patients, we identified commonly observed subcellular pathological phenotypes in

neuromelanin-containing neurons in the SN of PD patients (Fig. 5A), which may reflect different maturation stages of LB pathology. Based on our high-resolution observations in different experimental setups, combined with CARS data, we propose a hypothetical sequence of events in the formation of LBs in the SN (Fig. 5B). We speculate that different subcellular phenotypes of aSyn pathology are tightly coupled to the progressive collapse of protein degradation systems [47]. In healthy dopaminergic neurons, the basal proteolytic activity of the intracellular protein degradation systems – in particular the ubiquitin-proteasomal system (UPS) and chaperone-mediated autophagy (CMA)- are able to maintain protein homeostasis (Fig. 5B, step 1) [47]. In situations of increased protein burden, these systems are overloaded, and superfluous aSyn could start to aggregate with itself, other proteins, membranes and/or organelles [41]. Extensive phosphorylation of aSyn may take place at this point to stabilize the expanding mass of cellular debris and to activate the macrophagic machinery [38]. The alignment of aggregated material for focused macroautophagic clearance may explain the observed Ser129-p aSyn-immunopositive intracytoplasmic network (step 2). When the increase in macroautophagic activity is insufficient to reduce protein burden, aggrephagy – a specialized form of autophagy [44, 45] - is initiated by the sequestration of aggregated material into an expansive inclusion (step 3), which will grow and occupy an increasing cytoplasmic surface. At the point the inclusion cannot be cleared by proteolytic systems, cytoskeletal systems - major constituents in organizing cellular organelles and substructures - may be recruited to the LB to actively restructure the inclusion into a compact and stable morphology (step 4, 5). Interestingly, the idea of a restructuring of LBs during their maturation in a compaction-like manner has been proposed before in literature [2]. In the resulting onion skin-like morphology, highly aggregated proteins and lipids are centralized in the core of the structure, encapsulated by a ‘filamentous cage’ of Ser129-p aSyn and cytoskeletal components (step 5, 6). This hypothetical sequence of events in LB maturation could be

further explored in future experimental studies, for instance in cellular and animal models of aSyn aggregation in PD.

In line with previous studies using antibodies against CTT aSyn species, we found this PTM to localize towards the core of LBs [16, 27, 48]. CTT aSyn was repeatedly found to increase the propensity of aSyn to form amyloid aggregates *in vitro* [19-21, 23], and these observations together have led to the hypothesis that CTT aSyn plays a critical role in the initiation of protein aggregation [27]. However, as LBs were demonstrated to contain a medley of fragmented membranes and organelles [41], including components that are able to cleave aSyn, for instance caspase-1 [23], it cannot be ruled out that the enrichment of CTT aSyn in the core of LBs and LNs is the result of post-aggregation events.

Punctate cytoplasmic reactivity for 122CTT aSyn only showed limited co-localization with the Ser129-p immunoreactive network, and was independent of the presence of Lewy pathology (Fig. S6A). This PTM has been previously suggested to be a normal cellular process [19] and, indeed, presence of CTT aSyn was detected in brains of non-neurological control subjects by western blotting [16]. Interestingly, a substantial part of the 122CTT aSyn immunoreactive punctae in the cytoplasm was observed to localize at the outer membrane of VDAC/Porin-reactive mitochondria in diseased neurons from PD patients, but also in healthy neurons from non-neurological control subjects. This could be placed in line with the findings of the previously mentioned study, in which a 15kDa band corresponding with CTT aSyn, was observed in fractions enriched for lysosomes and mitochondria derived from SH-SY5Y cells expressing human WT α-synuclein [16]. Future experimental studies are necessary to explore the functional relevance of the co-occurence of 122CTT aSyn and mitochondria.

The immunoreactivity of aSyn antibodies often surrounded an unstained central core, which showed converging immunoreactivity for DAPI - a dye that binds to T-A-rich regions

of DNA [49]. This feature has already been reported before [50]. Although at this point the relevance of this observation is not clear, it was speculated that this may be the result of mitochondrial DNA incorporated in LBs [50]. Alternatively, DAPI may interact with certain aggregated proteins or lipids in the center of LBs. The limited immunoreactivity in the core of LBs may be the result of limited accessibility of antigen in this densely packed domain [40] or of masking or destruction of epitopes by its strong chemical environment. Importantly, LBs were shown to contain many (>300) proteins as identified by proteomics, which are predominantly centralized at the core of LBs based on our CARS results.

In summary, the present study provides a STED perspective on the architecture of Lewy pathology. Our results reveal a structured lamellar distribution of different forms of aSyn in nigral LBs and LNs. Our data suggest that LBs are actively regulated, structured encapsulations of aggregated proteins and lipids by a cage-like filamentous framework of Ser129-p aSyn and cytoskeletal components. Analysis of subcellular reactivity patterns led to the identification of different pathology-associated, Ser129-p aSyn-immunopositive subcellular phenotypes, suggesting a central role for Ser129-p aSyn in Lewy inclusion formation. The applied combination of well-characterized highly specific antibodies and super-resolution microscopy techniques in this study allowed an unprecedented detailed phenotyping of antibody-labeled subcellular pathology, which opens exciting opportunities for better characterization and understanding of PD pathophysiology.

Material and methods

Postmortem human brain tissue

Postmortem human brain tissue from clinically diagnosed and neuropathologically verified donors with advanced PD as well as non-demented controls was collected by the Netherlands Brain Bank (www.brainbank.nl). In compliance with all local ethical and legal

guidelines, informed consent for brain autopsy and the use of brain tissue and clinical information for scientific research was given by either the donor or the next of kin. Brains were dissected in compliance with standard operating protocols of the Netherlands Brain Bank and Brain Net Europe. The details of all donors included in this study are listed in Table S1. Most of these PD donors developed symptoms of dementia during their disease course (Table S1), while all had extensive α-synuclein pathology throughout the brain (Braak aSyn stage 5/6). Formalin-fixed paraffin-embedded (FFPE) tissue blocks of the substantia nigra (SN) and hippocampus - also containing part of the parahippocampal gyrus- from 9 donors with advanced PD and 6 non-demented controls (details in Table S1) were cut into 10 and 20 µm thick sections, which were utilized for immunohistochemistry and multiple labeling experiments. In addition, fresh-frozen tissue blocks of the SN from 5 patients with advanced PD were cut into 10 µm for CARS microscopy (Table S1).

Generation and initial characterization of antibodies towards specific epitopes of aSyn

A detailed overview of all utilized antibodies and their epitopes in this study is provided in Table S2. Generation and characterization of antibody 11A5 and syn105 was previously described [14, 15, 51]. Additional novel antibodies were generated by immunizing rabbits either with E. coli derived recombinant full length aggregated aSyn (asyn-055 and asyn-059) or KLH-conjugated peptides representing the C-terminus of 119CTT, 122CTT aSyn, or aSyn derived peptide phosphorylated at Ser129, respectively (for asyn-131, asyn-134, asyn-142). After screening of serum titers, standard B cell cloning was performed to generate rabbit monoclonal antibodies (mAbs). Recombinant mAbs were screened for binding to the peptides representing the aa1-60, 61-95, and aa96-140 by ELISA, respectively (for asyn-055 and asyn-059), or the C-terminus of aSyn119CTT, aSyn122CTT or phosphorylated at Ser129, respectively (for asyn-131, asyn-134, asyn-142), by ELISA and surface plasmon resonance (SPR). For asyn-055 and asyn-059, counter-screen by ELISA was performed with

beta- and gamma-synuclein. For asyn-131, and asyn-134 ELISA- or SPR-based counter-screenings using C-terminal elongated peptides were performed to identify mAbs highly specific for the C-termini of 119CTT or 122CTT aSyn. ELISA- or SPR based counter-screenings using the corresponding non-phosphorylated peptide were performed to identify asyn-142 as highly specific for aSyn phosphorylated at Ser129. All animal experiments followed highest animal welfare standards and were performed according to approved ethics protocols.

Antibodies included in the multiple labeling experiments were first optimized for immunohistochemistry. In the multiple labeling for the studied aSyn epitope, immunoreactivity patterns were validated using at least one different antibody raised against a similar epitope, with exception of the antibodies against 119CTT and the N-terminus of aSyn, as no other available antibody against a similar epitope could be integrated in the multiple labeling protocol.

Immunohistochemistry

Protocols for the antibodies against aSyn were optimized for light microscopy to characterize their immunoreactivity in human postmortem formalin-fixed paraffin-embedded brain tissue. All IHC protocols could be optimized without antigen retrieval procedure and without addition of Triton. The EnvisionTM+ kit (DAKO, Santa Clara, USA) was used as a high-sensitivity visualization system, with 3,3'-diaminobenzidine (DAB; 1:50 diluted in substrate buffer; DAKO) as the visible chromogen. Stained sections were analyzed using a Leica DM5000 B photo microscope (Leica Microsystems, Heidelberg, Germany). All brightfield images included in Figure S1 were acquired using a HC PL APO 63x1.40 oil objective using a Leica DFC450 digital camera (Leica Microsystems).

Development of triple and multiple labeling protocols

1. Immunoreactivity patterns of aSyn epitopes

Using immunofluorescent stainings, antibodies against different domains and PTMs of aSyn were co-visualized and their local distribution patterns were assessed in pathological structures and neurons. Triple labeling experiments, including DAPI and two antibodies against aSyn were performed to obtain insight into their distribution patterns. Moreover, to allow systematic comparison of distribution patterns of different aSyn epitopes, protocols were developed to visualize multiple (4 or 5) antibodies against aSyn in the same section.To validate findings from the initial multiple labeling experiments, different antibodies against similar epitopes were selected. This 'validation set' of antibodies was optimized for additional multiple labeling protocols. The sets of antibodies used in the different protocols are specified in Table S2. No antigen retrieval methods or permeabilization steps were applied in any of these experiments.

For each protocol, we made use of a combination of direct and indirect immunodetection methods. Several primary antibodies (specified in Table S2) were directly labeled with fluorochromes following standard protocols of different labeling kits (art. no. A20181, A20183, A20186, 21335 for labeling with Alexa 488, Alexa 546, Alexa 647, and biotin, respectively; Thermo Fisher Scientific, Waltham, USA). Each protocol started with an indirect immunolabeling using unlabeled primary antibodies raised in rabbit/mouse using their appropriate secondary antibodies (with different conjugates, specified in Table S2). Sections were then blocked for 1 hour in 5% normal rabbit serum and 5% normal mouse serum in PBS. After this, a biotinylated primary antibody (raised in mouse or rabbit) could be incubated, and visualized by fluophore-conjugated streptavidin. Then, sections were incubated in blocking solution (2% normal goat serum) containing the diluted directly labeled antibodies together with DAPI (1 µg/ml). Sections were mounted in Mowiol mounting solution using glass cover slips (Art. No.: 630-2746; Glaswarenfabrik Karl Hecht, Sondheim,

Germany). Negative control stainings lacking primary antibodies were performed to control for background/autofluorescence levels and aspecific staining. Single stainings using a directly labeled antibody against Ser129-p aSyn were scanned to determine autofluorescence levels of the studied morphological structures (LBs, LNs), which was found negligible under the applied scan settings.

Association CTT and Ser129-p aSyn with subcellular markers

In order to study the association of immunoreactivity of CTT and p-Ser129 aSyn with subcellular structures, additional multiple labeling protocols were further designed. Apart from the described antibodies against aSyn, these protocols also included some commercial antibodies as markers for subcellular structures, including mitochondria, ER and cytoskeletal proteins (Table S2). In these protocols, heat-induced epitope retrieval using citrate buffer (pH 6) and a permeabilization step (1hr incubation in 0.1% Triton-x) was included. Negative control stainings lacking primary antibodies were included to control for background/autofluorescence levels and aspecific staining.

Confocal laser scanning microscopy and stimulated emission depletion microscopy

CSLM and STED microscopy were performed using a Leica TCS SP8 STED 3X microscope (Leica Microsystems). All images were acquired using a HC PL APO CS2 100× 1.4 NA oil objective lens, with the resolution set to a pixel size of 20 nm x 20 nm. All signals were detected using gated hybrid detectors in counting mode. Sections were sequentially scanned for each fluorophore, by irradiation with a pulsed white light laser at different wavelengths (indicated in Table S2). Stacks in the Z-direction were made for each image. To obtain CSLM images of the DAPI signal, sections were irradiated with a solid state laser at a wavelength of 405 nm. For STED imaging, a pulsed STED laser line at a wavelength of 775 nm was used to deplete Abberior (580, 635P), Alexa (594, 647) or Li-Cor (680 nm)

fluorophores, while continuous wave (CW) STED lasers with wavelengths of 660 nm and 592 nm were used to deplete the Alexa 546 and Alexa 488 fluorophores, respectively. The DAPI signal was not depleted, so this channel was scanned at the same resolution as the CSLM images.

After scanning, deconvolution was performed using CMLE (for CSLM images) and GMLE algorithms in Huygens Professional (Scientific Volume Imaging; Huygens, The Netherlands) software. Images were adjusted for brightness/contrast in ImageJ (National Institute of Health, USA). 3D reconstructions were made using the LAS X 3D Visualization package (Leica Microsystems). Final figures were composed using Adobe Photoshop (CS6, Adobe Systems Incorporated).

Image processing and semi-quantitative analysis

Structures were classified and selected for inclusion in the analysis based on morphological grounds (specified in Results section). Additional criteria for inclusion were 1) the diameter of the structure (at least 5µm) and 2) the presence of specific signal for all channels (signal intensity of raw CSLM images substantially higher than autofluorescence or background levels under the applied scan settings). Based on this selection, distribution patterns of immunoreactivities could be analyzed on deconvolved CSLM images of 29 LBs in the SN of 8 patients with advanced PD (Table S1). Z-stacks were made for each structure, of which three frames in the central portion of the structure (Z length: 0.30µm; step size between frames: 0.15 µm) were selected to quantify the x-y distribution for different markers. For the analysis, a maximum Z-projection of these selected frames was first made in ImageJ. Subsequently, three 100 px (2µm) thick lines were drawn over the equatorial planes of the LBs [40] in ImageJ, along which signal intensities for each channel were measured. The intensity for each channel at each point was normalized to its maximum intensity in the same

structure, while the position along the diameter was expressed as % diameter. Normalized values were used to generate average line profiles per morphological structure. The center of the LB was defined as the origin of the structure [40]. The position in the LB with the maximum intensity was determined per channel. Absolute positions, with low values corresponding to positions close to the origin of the LB and high values to positions at their periphery, were compared between channels (Test: One way ANOVA; post-hoc: Bonferroni).

Coherent anti-Stokes Raman scattering

The workflow used for CARS microscopy is outlined in Figure S7. The detection of the lipid and protein distribution was performed on native, dried samples [52, 53]. A commercial setup (Leica TCS SP5 II CARS, Leica Microsystems) was used with an HCX IRAPO L25X/0.95W (Leica Microsystems) objective. For the lipid distribution intensity images were taken at 2850 cm^{-1} (Pump-wavelength 816 nm, Stokes-wavelength 1064 nm) and for the protein distribution intensity images at 2930 cm^{-1} (Pump-wavelength 810 nm, Stokes-wavelength 1064 nm). The laser power at the sample was 28 mW (Pump) and 21 mW (Stokes). Integration times of 34 s per image with a pixel dwell time of 32 µs, 1024x1024 pixels and a spatial resolution of 300 nm were used [54]. After the label-free detection of the lipid and protein distribution, immunofluorescent stainings were performed on the same sections (Fig. S7). Tissue sections were fixed in 4% formaldehyde for 10 minutes and stained for aSyn, using two primary antibodies raised against aSyn (LB509; ab27766, Abcam, Cambridge, UK) and Ser129-p aSyn (ab59264, Abcam) and their appropriate secondary antibodies. After this, sections were incubated in Sudan Black for 30 min and mounted in Mowiol. For fluorescence detection, a commercial setup (Leica TCS SP5 II CARS, Leica Microsystems, Heidelberg, Germany) was used. Data evaluation was done in Matlab with the Image Processing and Statistics toolboxes (The Mathworks, Inc., Mass.,USA). First, large overview CARS-intensity and fluorescence images were manually overlaid by comparison of

morphological features. The distribution of aSyn, proteins and lipids was identified by the overlay of both fluorescence images (Fig. S8). Therewith, autofluorescence of the surrounding tissue and the fluorescent signal of the aSyn-immunopositive inclusions could be separated. The inclusion bodies were manually identified based on morphology. Only inclusions with a diameter of 5-20 µm were included for analysis.

Image processing and analysis of CARS images

For an objective evaluation of CARS intensity of aSyn-immunopositive inclusion bodies, the mean CARS intensity of the direct surrounding, a donut with a width of 3.5 µm, was compared with the CARS intensity of the inclusion (Fig. S8A, light blue and yellow area). The areas of aSyn-immunopositivity were transferred into the CARS-intensity images. Areas with no intensity in the CARS intensity images (holes) were excluded by intensity thresholding. CARS-pixel-intensities higher than 1.4 times the mean CARS-intensity of the surrounding were defined as higher protein/lipid content, which was determined based on pilot measurements in a subset of (~40) aSyn-positive inclusions. The ratio between the CARS-pixel-intensities of the LB and the mean CARS intensity of the surrounding were calculated and the areas with higher protein/lipid content were marked in red (Fig. S8). Morphological filtering and image processing were performed in Matlab R2017a, MathWorks.

Acknowledgements

We are grateful to all individuals that donated their brain to the Netherlands Brain Bank (NBB; www.brainbank.nl). We thank the team of the NBB, in particular Michiel Kooreman, for their cooperation and their help in the selection of brain tissue. We thank the Advanced Optical Microscopy Core O|2 (www.ao2m.amsterdam) for support with STED imaging.

Further, we thank Lidia Janota for performing immunofluorescent stainings of the tissue sections used for CARS microscopy.

Author contributions

T.M. and C.M. performed immunohistochemistry and multiple labeling experiments. T.M., C.M., E.T., J.K. and W.vdB. performed STED imaging, as well as processing and analysis of images. D.N., D.P., S.EM. and K.G. performed experiments and data analysis for CARS microscopy. D.M. performed the labeling of antibodies for multiple labeling experiments and contributed to the experimental design. M.B., W.Z., R.B., O.M., K.K., S.H., M.H., T.K., M.R., S.D. selected and characterized the aSyn antibodies. T.M., W.vdB, J.G.and M.B. designed research, analyzed and interpreted the data, and contributed to writing the manuscript.

Competing financial interests

The authors declare no competing interests. D.M., O.M., K.K., S.H., M.H., T.K., M.R., S.D., and M.B. are full-time employees of Roche/F. Hoffmann–La Roche Ltd, and they may additionally hold Roche stock/stock options. W.Z. and R.B. are full-time employees of Prothena Biosciences Inc. **Corresponding author:**

Correspondence to: Wilma van de Berg (wdj.vandeberg@vumc.nl)

References

1. Wakabayashi, K., *et al.* The Lewy body in Parkinson's disease and related neurodegenerative disorders. *Mol Neurobiol* **47**, 495-508 (2013).

2. Kuusisto, E., Parkkinen, L. & Alafuzoff, I. Morphogenesis of Lewy bodies: dissimilar incorporation of alpha-synuclein, ubiquitin, and p62. *J Neuropathol Exp Neurol* **62**, 1241-1253 (2003).

3. Spillantini, M.G., Crowther, R.A., Jakes, R., Hasegawa, M. & Goedert, M. alpha-Synuclein in filamentous inclusions of Lewy bodies from Parkinson's disease and dementia with lewy bodies. *Proc Natl Acad Sci U S A* **95**, 6469-6473 (1998).

4. Maroteaux, L., Campanelli, J.T. & Scheller, R.H. Synuclein: a neuron-specific protein localized to the nucleus and presynaptic nerve terminal. *J Neurosci* **8**, 2804-2815 (1988).

5. Iwai, A.*, et al.* The precursor protein of non-A beta component of Alzheimer's disease amyloid is a presynaptic protein of the central nervous system. *Neuron* **14**, 467-475 (1995).

6. George, J.M., Jin, H., Woods, W.S. & Clayton, D.F. Characterization of a novel protein regulated during the critical period for song learning in the zebra finch. *Neuron* **15**, 361-372 (1995).

7. Burre, J., Sharma, M. & Sudhof, T.C. Cell Biology and Pathophysiology of alpha-Synuclein. *Cold Spring Harb Perspect Med* **8** (2018).

8. Eliezer, D., Kutluay, E., Bussell, R., Jr. & Browne, G. Conformational properties of alpha-synuclein in its free and lipid-associated states. *J Mol Biol* **307**, 1061-1073 (2001).

9. Eliezer, D. The mysterious C-terminal tail of alpha-synuclein: nanobody's guess. *J Mol Biol* **425**, 2393-2396 (2013).

10. Oueslati, A., Fournier, M. & Lashuel, H.A. Role of post-translational modifications in modulating the structure, function and toxicity of alpha-synuclein: implications for Parkinson's disease pathogenesis and therapies. *Prog Brain Res* **183**, 115-145 (2010).

11. Lashuel, H.A., Overk, C.R., Oueslati, A. & Masliah, E. The many faces of alpha-synuclein: from structure and toxicity to therapeutic target. *Nat Rev Neurosci* **14**, 38-48 (2013).

12. Mor, D.E., Ugras, S.E., Daniels, M.J. & Ischiropoulos, H. Dynamic structural flexibility of alpha-synuclein. *Neurobiol Dis* **88**, 66-74 (2016).

13. Fujiwara, H., *et al.* alpha-Synuclein is phosphorylated in synucleinopathy lesions. *Nat Cell Biol* **4**, 160-164 (2002).

14. Anderson, J.P., *et al.* Phosphorylation of Ser-129 is the dominant pathological modification of alpha-synuclein in familial and sporadic Lewy body disease. *J Biol Chem* **281**, 29739-29752 (2006).

15. Games, D., *et al.* Axonopathy in an alpha-synuclein transgenic model of Lewy body disease is associated with extensive accumulation of C-terminal-truncated alpha-synuclein. *Am J Pathol* **182**, 940-953 (2013).

16. Muntane, G., Ferrer, I. & Martinez-Vicente, M. alpha-synuclein phosphorylation and truncation are normal events in the adult human brain. *Neuroscience* **200**, 106-119 (2012).

17. Hasegawa, M., *et al.* Phosphorylated alpha-synuclein is ubiquitinated in alpha-synucleinopathy lesions. *J Biol Chem* **277**, 49071-49076 (2002).

18. Baba, M., *et al.* Aggregation of alpha-synuclein in Lewy bodies of sporadic Parkinson's disease and dementia with Lewy bodies. *Am J Pathol* **152**, 879-884 (1998).

19. Li, W., *et al.* Aggregation promoting C-terminal truncation of alpha-synuclein is a normal cellular process and is enhanced by the familial Parkinson's disease-linked mutations. *Proc Natl Acad Sci U S A* **102**, 2162-2167 (2005).

20. Liu, C.W., *et al.* A precipitating role for truncated alpha-synuclein and the proteasome in alpha-synuclein aggregation: implications for pathogenesis of Parkinson disease. *J Biol Chem* **280**, 22670-22678 (2005).

21. Murray, I.V., *et al.* Role of alpha-synuclein carboxy-terminus on fibril formation in vitro. *Biochemistry* **42**, 8530-8540 (2003).

22. Hoyer, W., Cherny, D., Subramaniam, V. & Jovin, T.M. Impact of the acidic C-terminal region comprising amino acids 109-140 on alpha-synuclein aggregation in vitro. *Biochemistry* **43**, 16233-16242 (2004).

23. Wang, W., *et al.* Caspase-1 causes truncation and aggregation of the Parkinson's disease-associated protein alpha-synuclein. *Proc Natl Acad Sci U S A* **113**, 9587-9592 (2016).

24. Oueslati, A. Implication of Alpha-Synuclein Phosphorylation at S129 in Synucleinopathies: What Have We Learned in the Last Decade? *J Parkinsons Dis* **6**, 39-51 (2016).

25. Schmid, A.W., Fauvet, B., Moniatte, M. & Lashuel, H.A. Alpha-synuclein post-translational modifications as potential biomarkers for Parkinson disease and other synucleinopathies. *Mol Cell Proteomics* **12**, 3543-3558 (2013).

26. Dehay, B., *et al.* Targeting alpha-synuclein for treatment of Parkinson's disease: mechanistic and therapeutic considerations. *Lancet Neurol* **14**, 855-866 (2015).

27. Prasad, K., Beach, T.G., Hedreen, J. & Richfield, E.K. Critical role of truncated alpha-synuclein and aggregates in Parkinson's disease and incidental Lewy body disease. *Brain Pathol* **22**, 811-825 (2012).

28. Alafuzoff, I., *et al.* Assessment of alpha-synuclein pathology: a study of the BrainNet Europe Consortium. *J Neuropathol Exp Neurol* **67**, 125-143 (2008).

29. Forno, L.S. Neuropathology of Parkinson's disease. *J Neuropathol Exp Neurol* **55**, 259-272 (1996).

30. Duffy, P.E. Phase and electron microscopic observations of Lewy bodies and melanin granules in the substantia nigra and locus caeruleus in Parkinson's disease. *Journal of Neuropathology and Experimental Neurology* **24**, 398 (1965).

31. Kovacs, G.G., *et al.* An antibody with high reactivity for disease-associated alpha-synuclein reveals extensive brain pathology. *Acta Neuropathol* **124**, 37-50 (2012).

32. Puska, G., *et al.* Lysosomal response in relation to alpha-synuclein pathology differs between Parkinson's disease and multiple system atrophy. *Neurobiol Dis* **114**, 140-152 (2018).

33. Lue, L.F., *et al.* Biochemical increase in phosphorylated alpha-synuclein precedes histopathology of Lewy-type synucleinopathies. *Brain Pathol* **22**, 745-756 (2012).

34. Volpicelli-Daley, L.A., *et al.* Exogenous alpha-synuclein fibrils induce Lewy body pathology leading to synaptic dysfunction and neuron death. *Neuron* **72**, 57-71 (2011).

35. Rezaei-Ghaleh, N., Amininasab, M., Kumar, S., Walter, J. & Zweckstetter, M. Phosphorylation modifies the molecular stability of beta-amyloid deposits. *Nat Commun* **7**, 11359 (2016).

36. Paleologou, K.E., *et al.* Phosphorylation at Ser-129 but not the phosphomimics S129E/D inhibits the fibrillation of alpha-synuclein. *J Biol Chem* **283**, 16895-16905 (2008).

37. Dahmene, M., Berard, M. & Oueslati, A. Dissecting the Molecular Pathway Involved in PLK2 Kinase-mediated alpha-Synuclein-selective Autophagic Degradation. *J Biol Chem* **292**, 3919-3928 (2017).

38. Oueslati, A., Schneider, B.L., Aebischer, P. & Lashuel, H.A. Polo-like kinase 2 regulates selective autophagic alpha-synuclein clearance and suppresses its toxicity in vivo. *Proc Natl Acad Sci U S A* **110**, E3945-3954 (2013).

39. Kanazawa, T., *et al.* Pale neurites, premature alpha-synuclein aggregates with centripetal extension from axon collaterals. *Brain Pathol* **22**, 67-78 (2012).

40. Gai, W.P., *et al.* In situ and in vitro study of colocalization and segregation of alpha-synuclein, ubiquitin, and lipids in Lewy bodies. *Exp Neurol* **166**, 324-333 (2000).

41. Shahmoradian, S.H., *et al.* Lewy pathology in Parkinson's disease consists of a crowded organellar membranous medley. *bioRxiv* (2017).

42. den Hartog Jager, W.A. Sphingomyelin in lewy inclusion bodies in parkinson's disease. *Archives of Neurology* **21**, 615-619 (1969).

43. Ghio, S., Kamp, F., Cauchi, R., Giese, A. & Vassallo, N. Interaction of alpha-synuclein with biomembranes in Parkinson's disease--role of cardiolipin. *Prog Lipid Res* **61**, 73-82 (2016).

44. Hyttinen, J.M.*, et al.* Clearance of misfolded and aggregated proteins by aggrephagy and implications for aggregation diseases. *Ageing Res Rev* **18**, 16-28 (2014).

45. Kopito, R.R. Aggresomes, inclusion bodies and protein aggregation. *Trends Cell Biol* **10**, 524-530 (2000).

46. Olanow, C.W., Perl, D.P., DeMartino, G.N. & McNaught, K.S. Lewy-body formation is an aggresome-related process: a hypothesis. *Lancet Neurol* **3**, 496-503 (2004).

47. Moors, T.*, et al.* Lysosomal Dysfunction and alpha-Synuclein Aggregation in Parkinson's Disease: Diagnostic Links. *Mov Disord* **31**, 791-801 (2016).

48. Dufty, B.M.*, et al.* Calpain-cleavage of alpha-synuclein: connecting proteolytic processing to disease-linked aggregation. *Am J Pathol* **170**, 1725-1738 (2007).

49. Williamson, D.H. & Fennell, D.J. The use of fluorescent DNA-binding agent for detecting and separating yeast mitochondrial DNA. *Methods Cell Biol* **12**, 335-351 (1975).

50. Power, J.H., Barnes, O.L. & Chegini, F. Lewy Bodies and the Mechanisms of Neuronal Cell Death in Parkinson's Disease and Dementia with Lewy Bodies. *Brain Pathol* **27**, 3-12 (2017).

51. Games, D.*, et al.* Reducing C-terminal-truncated alpha-synuclein by immunotherapy attenuates neurodegeneration and propagation in Parkinson's disease-like models. *J Neurosci* **34**, 9441-9454 (2014).

52. El-Mashtoly, S.F.*, et al.* Automated identification of subcellular organelles by coherent anti-stokes Raman scattering. *Biophys J* **106**, 1910-1920 (2014).

53. Petersen, D.*, et al.* Virtual staining of colon cancer tissue by label-free Raman micro-spectroscopy. *Analyst* **142**, 1207-1215 (2017).

54. Niedieker, D., *et al.* Label-free identification of myopathological features with coherent anti-Stokes Raman scattering. *Muscle Nerve* (2018).

Figure legends

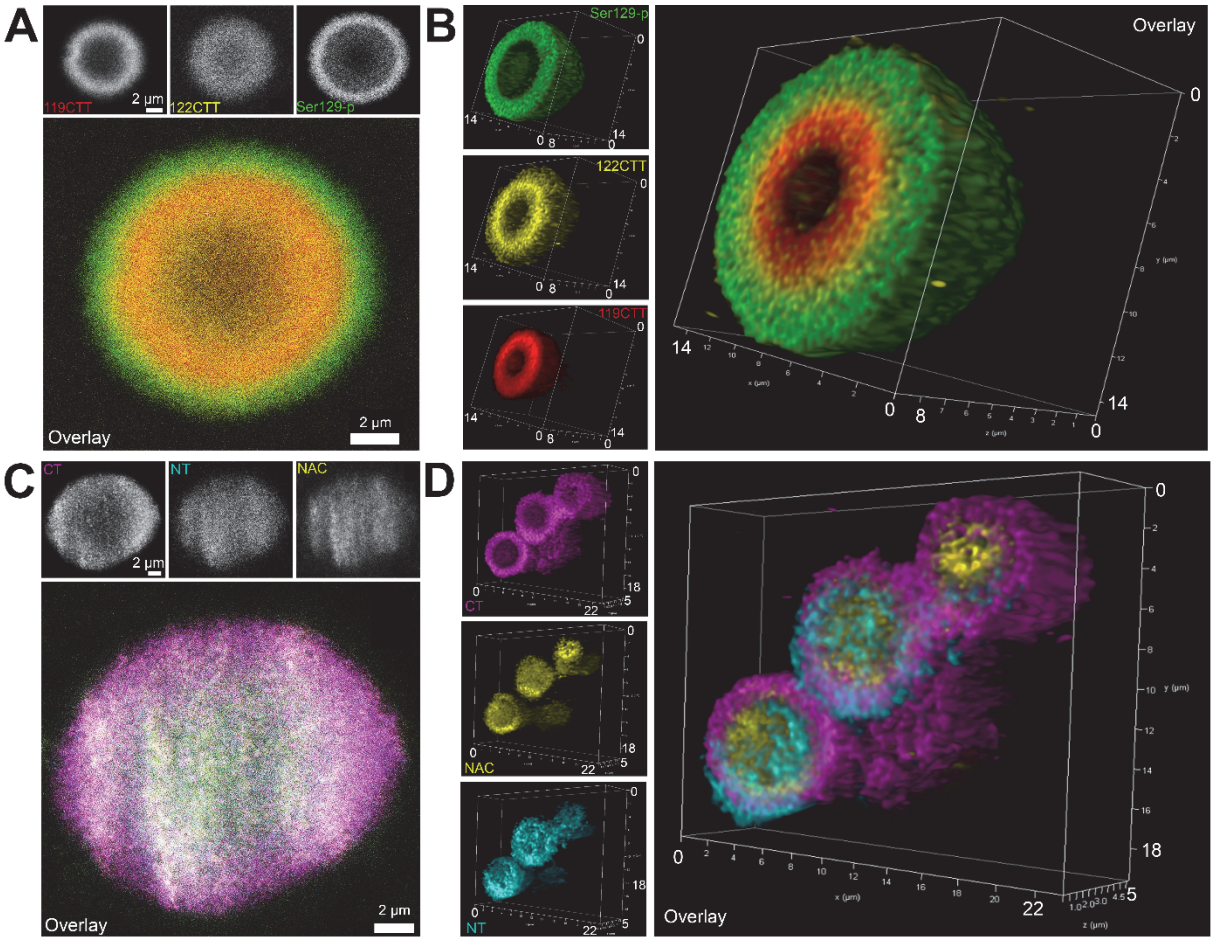

Fig 1: Lamellar distribution patterns of aSyn PTMs and aSyn domains in LBs. A: Triple labeling of aSyn PTMs: representative raw STED image of a nigral LBin patient PD7, showing immunoreactivity for Ser129-p aSyn at the periphery of the LB while 119CTT and 122 CTT aSyn are localized in the core of the structure. **B:** 3D reconstruction based on deconvolved CSLM images showing the lamellar distribution of different aSyn PTMs in a nigral LB in patient PD6. **C:** Triple labeling of different aSyn domains: raw STED image of a nigral LB, showing immunoreactivity for CT aSyn at the periphery of the LB and NT and NAC aSyn staining in the core of the structure, taken in the SN of patient PD8. **C:** 3D reconstruction based on deconvolved CSLM images showing different localization for different aSyn domains in a complex of three LBs in the SN of patient PD8.

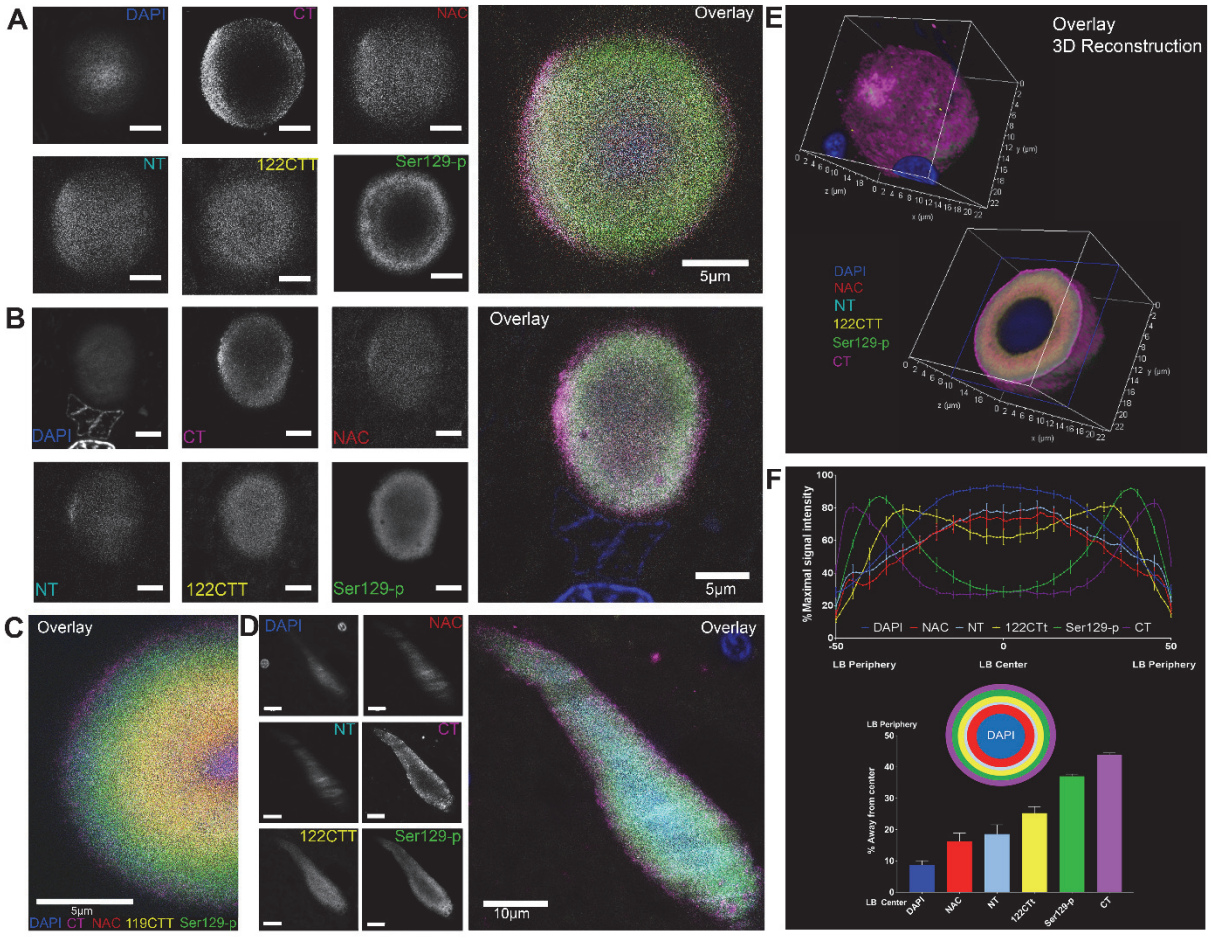

Fig 2: Onion skin-like orchestration of different aSyn epitopes in nigral LBs and LNs. **A, B:** Raw STED-images showing immunoreactivities for different aSyn epitopes in onion skin-type LBs in the SN of patient PD1 (**A)** and PD5 (**B**). Immunoreactivities for CT and Ser129-p aSyn are localized at the periphery of the structures, while NT, NAC and 122CTT reactivities were present mainly in their core. **C:** Raw STED image of protocol including an antibody against 119CTT aSyn, taken in the SN of patient PD5. **D:** Raw STED image of a dystrophic LN in the SN of patient PD7. **E:** 3D reconstruction of an entire nigral LB based on deconvolved CSLM images in patient PD1. **F:** Top: Average line profile (±SEM) for 29 onion skin-like LBs measured in the SN of 8 PD patients, showing a separation of peak intensities indicating a systematic build-up of LBs. Bottom: Bar graph showing the centrality of peak

intensities for aSyn epitopes. Middle: a schematic depiction of the lamellar architecture of LBs. **A-C:** Scale bar = 5 µm; **D:** Scale bar = 10 µm

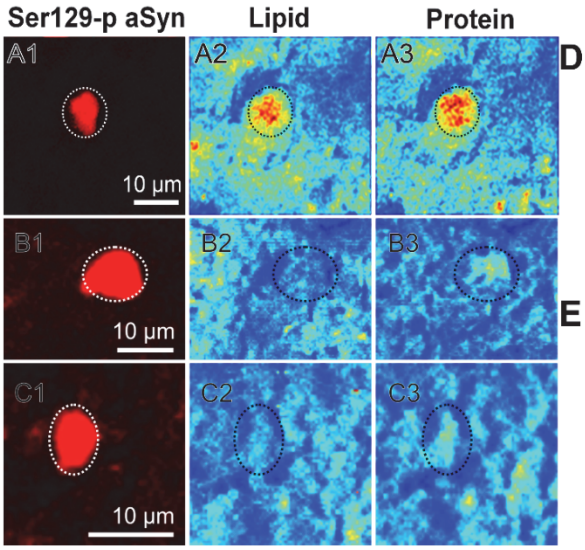

D

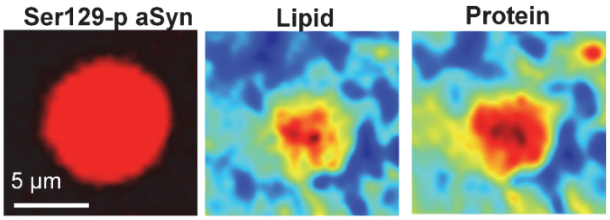

E

Patient ID	1	2	3	4	5	Total (%)
Total aSyn-positive inclusions	9	8	15	14	11	57
Higher protein concentration	7	3	10	9	8	37/57 (65)
Higher lipid concentration	4	3	4	5	4	20/57 (35)
Lipid in center	1	3	2	5	3	14/20 (70)
Protein in center	3	3	6	9	7	28/37 (76)
Lipid and protein in center	1	3	2	5	3	14/20 (70)

Fig 3: Protein and lipid distribution of nigral LBs. A-C: Different compositions of LBs as identified by CARS microscopy. The fluorescence images of Ser129-p aSyn of different LB types are depicted (first column). CARS signal intensities at 2850 cm^{-1} and 2930 cm^{-1} shows lipid (second column) and protein (third column) distributions, respectively. Low CARS-intensities are depicted in blue, whereas high intensities are depicted in red. LBs with different compositions were identified: LBs with high CARS intensities for proteins and lipids compared to the direct environment (A1-3), with high CARS intensity for proteins but not lipids (B1-3), and with low CARS intensity for proteins and lipids (C1-3). **D:** Representative image of a LB with high protein and lipid signal centralized in the structure. **E:** Numbers and proportions of nigral LBs with high (centralized) lipids or proteins per patient.

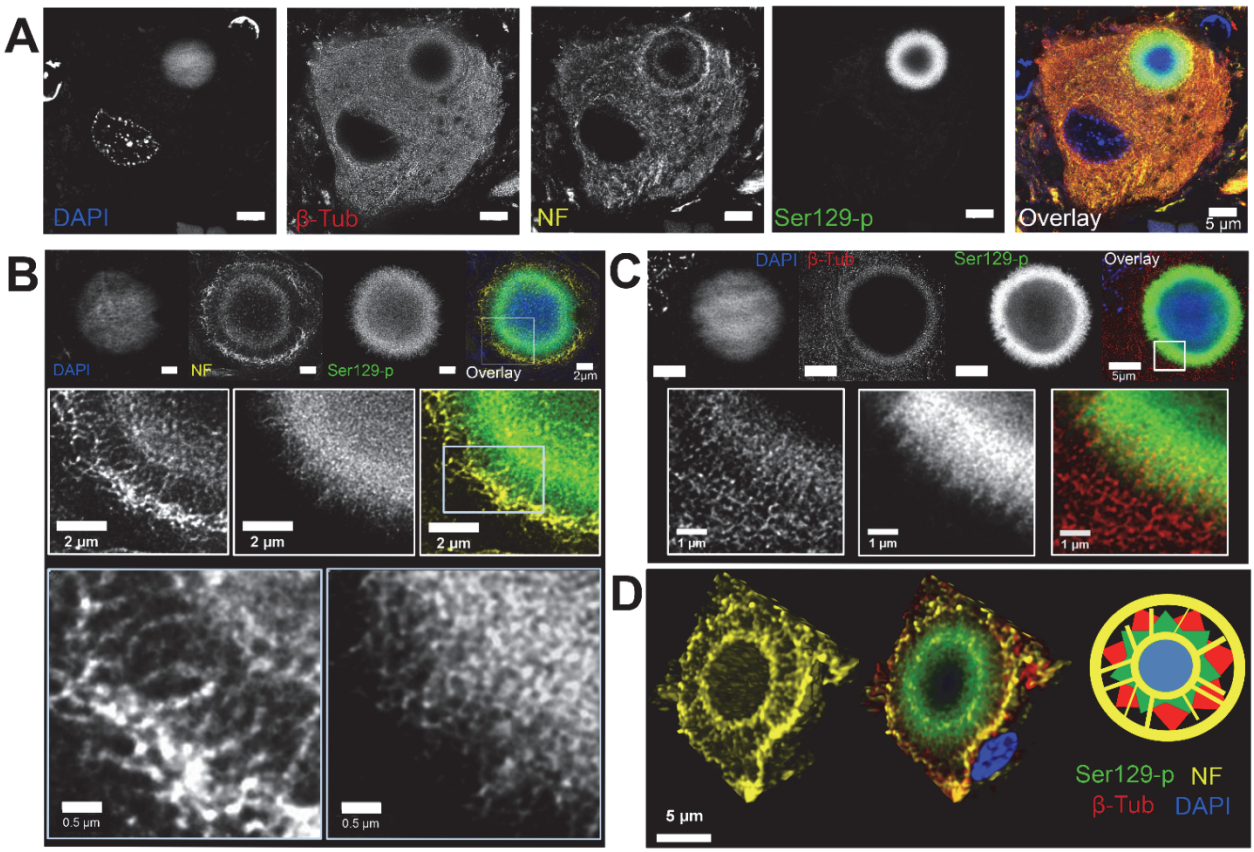

Fig 4: Ser129-p aSyn forms filamentous framework with cytoskeletal components at the periphery of nigral LBs. **A:** Deconvolved STED image of neuromelanin-containing dopaminergic neuron in the SN with LB. Immunoreactivity for beta-tubulin and neurofilament (in two rings) is observed at the periphery of the LB. **B:** Deconvolved STED images showing the detailed structure of neurofilament in a onion skin-type LB at different magnifications. Two tangentially oriented rings of immunoreactive filaments are connected by radiating filaments. Ser129-p aSyn shows a corona of immunoreactivity, revealing filament-like structures with a radial orientation. **C:** Deconvolved STED images showing filamentous beta-tubulin reactivity at the periphery of a LB. **D:** Left: 3D reconstruction of the localization of Ser129-p aSyn and cytoskeletal components in a nigral LB, highlighting the wheel-like structure of neurofilament. Right: schematic summary of the results. NF: neurofilament; β-Tub: beta-tubulin.

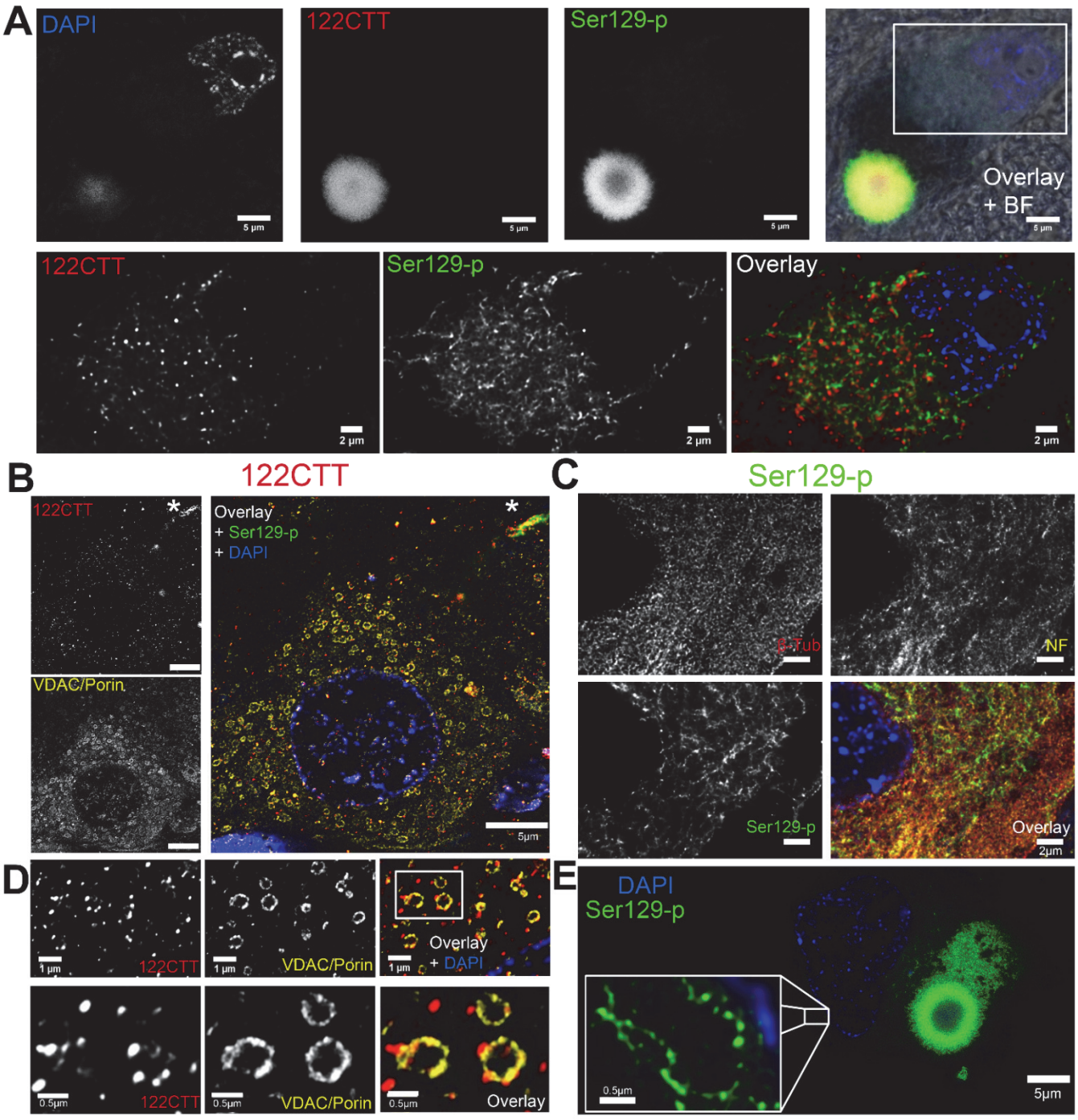

Fig 5: Subcellular manifestation of 122CTT and Ser129-p aSyn. A: Overview of a neuromelanin-containing dopaminergic neuron in the SN with a LB (first row) and a zoom-in on its cytoplasm (second row). Signal intensity for 122CTT and Ser129-p aSyn was highest in the LB, suggesting an enrichment for these PTMs in pathological inclusions. However, cytoplasmic reactivity could also be observed, showing different manifestations for 122CTT and Ser129-p aSyn. **B:** Cytoplasmic 122CTT immunopositive punctae showed association

with staining patterns for VDAC/Porin-immunopositive mitochondria in the hippocampal CA2 of a PD patient. Staining was also observed in a LN (indicated with an asterix). **C:** Ser129-p aSyn immunopositive fibrous network showed limited co-localization with markers for beta-tubulin and neurofilament in the cytoplasm of a melanin-containing dopaminergic neuron in the SN of a PD patient. **D:** Localization of 122CTT immunopositive punctae at the outer membrane of mitochondria in the hippocampal CA2 of a PD patient at different magnifications. **E:** Dopaminergic neuron in the SN containing a combination of expansive-appearing inclusion and onion-skin type LB surrounded by aSer129-p aSyn immunoreactive filamentous network. Insert: zoom in of fibers close to the nucleus, showing Ser129-p aSyn immunopositive filamentous structures, with a diameter of ~70nm. **A:** Deconvolved CSLM images; **B-E:** deconvolved STED images.

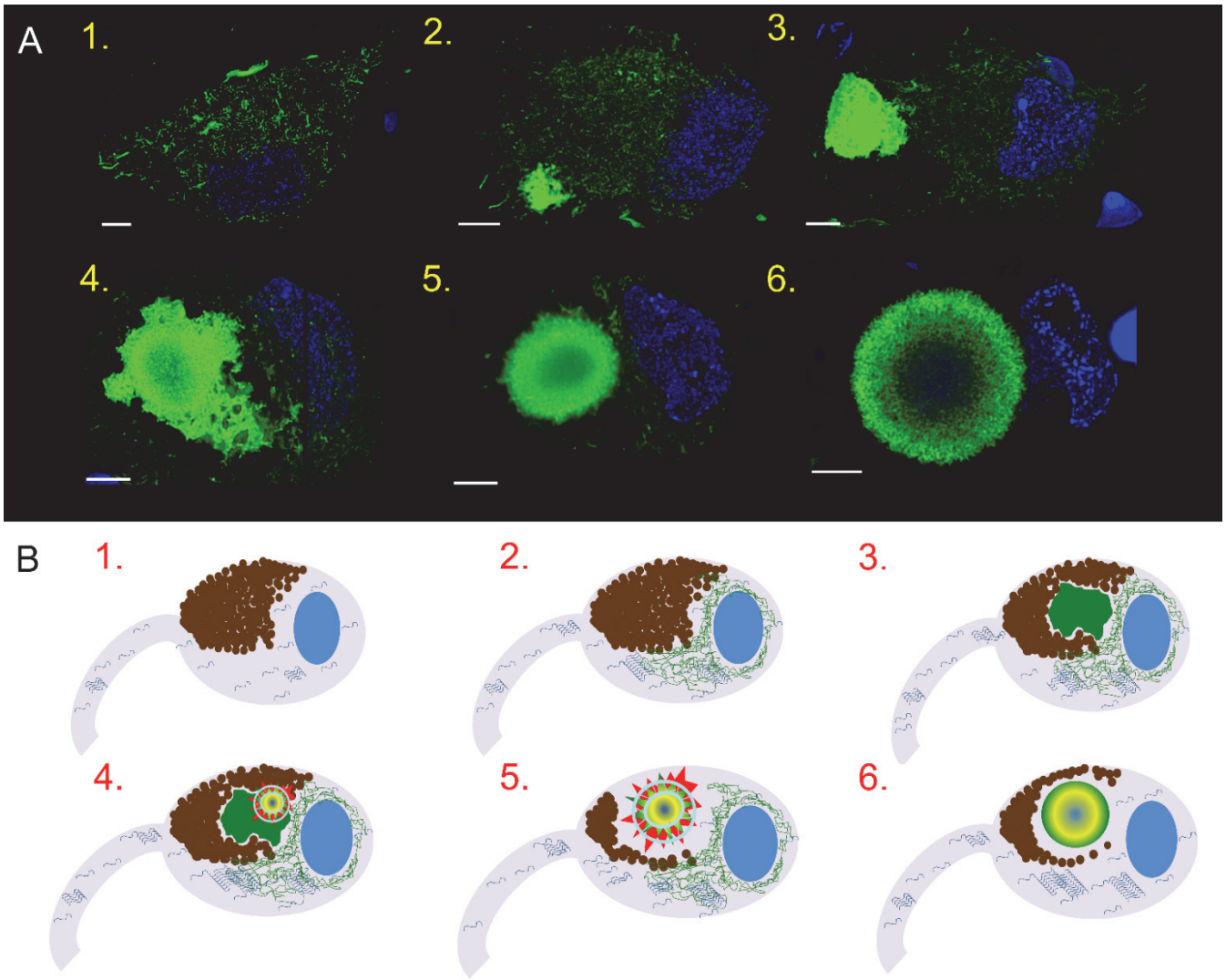

Figure 6: Many intracytoplasmic faces of Ser129-p aSyn hint to different maturation stages of LBs. A) Different patterns of Ser129-p aSyn immunoreactivity in neuromelanin-containing dopaminergic cells in the SN of PD patients, based on Ser129-p aSyn immunoreactivity patterns. Images are 2D visualizations of 3D reconstructions based on CSLM image stacks. Entire cells were scanned. The following cellular phenotypes were commonly observed: 1) neurons containing intracytoplasmic network but without apparent inclusion; 2,3) neurons with intracytoplasmic network and smaller (2) and larger (3) expansive-appearing inclusions; 4) neuron with intracytoplasmatic network and combination of an expansive-appearing inclusion and compact onion skin-type LBs; 5) neuron with

intracytoplasmic network and onion skin-type LB; 6) neuron without intracytoplasmic network and onion skin-type LB. Scale bars: 5µm. **B)** Hypothetical sequence of events in LB formation in dopaminergic neurons in the SN of PD patients, based on Ser129-p aSyn immunoreactivity patterns (visualized in green; detailed explanation in text). 1) Neuromelanin-containing neuron with protein homeostasis; 2) alignment of Ser129-p aSyn; 3) sequestration of proteins into expanding cytoplasmic inclusion; 4,5) cytoskeletal structures are recruited and to restructure the inclusion in a compaction-like manner into a multilamellar onion skin-type LB morphology (6)

Supplementary material

Table S1: Donor tissue included in different experiments. Abbreviations: CD: clinical diagnosis; CERAD: CERAD age-related score for neuritic plaques; Exp: Experiments: 1) FFPE sections used for immunofluorescence multiple labeling experiments; 2) Snap-frozen sections used for CARS microscopy, PDD: PD with dementia; AD: Alzheimer's Disease

ID	Diag.	Age at death	Sex	Braak LB score	Braak NFT score	CERAD score	Age of diagnosis	Age at onset dementia	Exp	Figure
PD1	PDD	80	M	6	1	B	55	73	1	2A,E
PD2	PDD	72	M	6	1	O	64	69	1	S1A
PD3	PD	72	M	6	1	A	57	-	1	-
PD4	PDD	80	M	6	1	O	69	77	1	S1B; 4B,D; S3A,C
PD5	PD	77	M	6	2	O	60	-	1	2B,C
PD6	PD+AD	74	M	6	4	B	64	73	1	1B; 4A,B,D; 5A,C; S5
PD7	PDD	66	F	6	1	A	57	64	1	1A; 2D; 4C,E;5E; S3D; S2;S4
PD8	PDD	87	M	6	3	C	77	86	1	1C
PD9	PD	67	F	6	1	B	60	-	2	-
PD10	PDD	81	M	6	2	O	72	79	2	3C
PD11	PDD	74	M	5	3	O	67	71	2	3D
PD12	PDD	76	M	6	1	B	66	71	2	3A, B
PD13	PDD	83	M	6	1	B	78	80	1,2	-
C1	C	83	F	0	3	A	-	-	1	S6A
C2	C	80	M	0	1	B	-	-	1	-
C3	C	89	F	0	1	A	-	-	1	S6B
C4	C	84	F	0	1	O	-	-	1	-
C5	C	81	M	0	2	O	-	-	1	-
C6	C	70	F	0	2	A	-	-	1	-

Table S2: Antibodies used in final multiple labeling experiments with direct and indirect detection. Exp: experiment. 1) light microscopy; 2) multiple labeling of aSyn epitopes; 3) multiple labeling of aSyn epitopes with CTT119; 4) multiple labeling of aSyn epitiopes, validation set; 5) multiple labeling PTMs and cytoskeletal markers; 6) multiple labeling PTMs + ER; 7) multiple labeling PTMs and mitochondria. *: biotinylated antibody used in multiple labeling protocols. **Abbreviation:** AB: antibody; Exp: experiment; Ref: reference for additional information on AB characterization; d.l.: antibody directly labeled with fluophore

Epitope	AB ID (Cat #)	Source	Host species	Exp	Fluorochrome	STED depletion wavelength	Ref
Ser129-p	11A5	Prothena	Mouse	1,2,5,6,7	Alexa 488(d.l.)/Alexa 488	592	[14]
Ser129-p	asyn-142 (7E2)	Roche	Rabbit	1,4,5,6,7	Alexa 488 (d.l.)/Alexa 488	592	
122CTT	Syn105	Prothena	Rabbit	1,2*,5*,6*,7	Alexa 547 Alexa 594/Abberior 635p	660 775	[15]
122CTT	asyn-134 (5H7)	Roche	Rabbit	1,4*,5*,6*,7	Alexa 547 Alexa 594/Abberior 635p	660 775	
119CTT	asyn-131 (2D9)	Roche	Rabbit	1,3,5,7	Alexa 647 (d.l.)	775	
NT (40-55)	23E8	Prothena	Mouse	1,4	Alexa 647 (d.l.)	775	
NAC	asyn-055	Roche	Rabbit	1,2	Alexa 488 Li-Cor 680	592 775	
NAC	asyn-059	Roche	Rabbit	1,4	Li-Cor 680	775	
CT	5C1	Prothena	Mouse	1,2	Alexa 594	775	[51]
CT	SC-211	Santa Cruz	Mouse	1,4	Alexa 594	775	
KM-51	MONX10738	Monosan	Mouse	1	- (only light microscopy)	-	
Intermediate neurofilament	837801	BioLegend	Mouse	5,6	Abberior 580	775	
Beta-tubulin	ab18207	Abcam	Rabbit	5	Abberior 635p	775	
Calreticulin	ab2907	Abcam	Rabbit	6	Abberior 635p	775	
VDAC/Porin	ab14734	Abcam	Mouse	7	Abberior 580	775	

Table S3: Different distribution of peak intensities between aSyn epitopes. Overview of p-values from ANOVA test, adjusted by Bonferroni's test for multiple comparisons.

	DAPI	**NAC**	**NT**	**122CTT**	**Ser129-p**	**CT**
DAPI	**x**	0.1042	0.0067	<0.0001	<0.0001	<0.0001
NAC	0.1042	**x**	0.9999	0.0196	<0.0001	<0.0001
NT	0.0067	0.9999	**x**	0.2481	<0.0001	<0.0001
122CTT	<0.0001	0.0196	0.2481	**x**	0.0005	<0.0001
Ser129-p	<0.0001	<0.0001	<0.0001	0.0005	**x**	0.2171
CT	<0.0001	<0.0001	<0.0001	<0.0001	0.2171	**x**

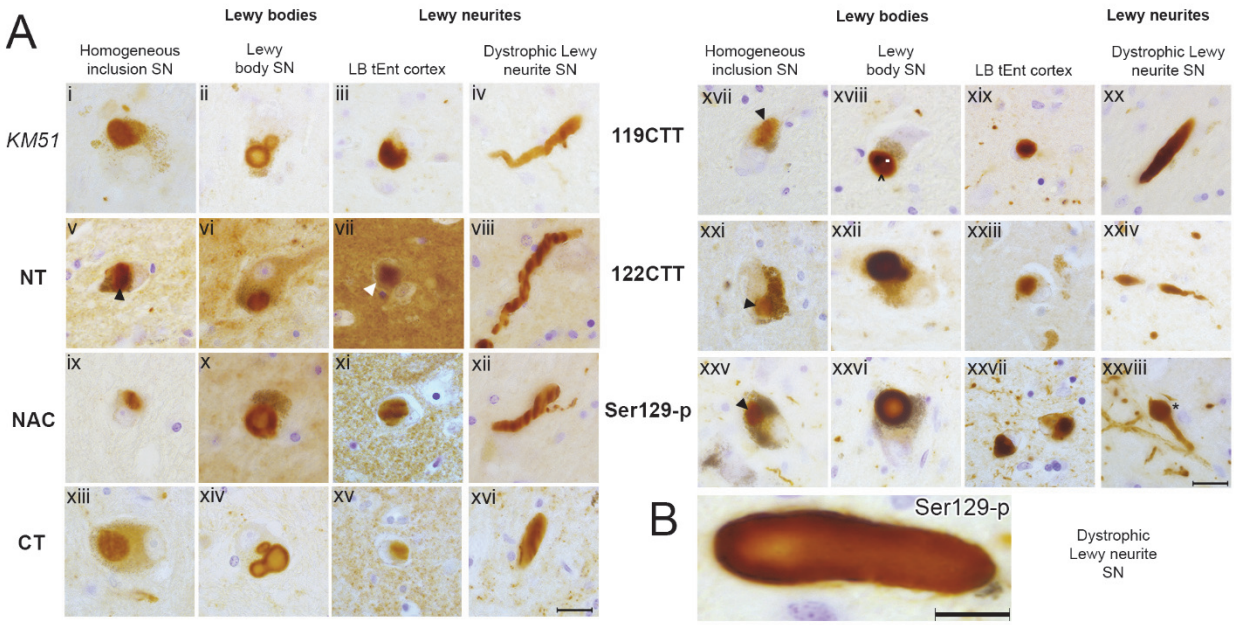

Fig S1: Characterization of immunoreactivity for antibodies against aSyn domains and PTMs in postmortem brains with advanced PD pathology. A: Representative brightfield images for selected morphological structures detected by antibodies against different aSyn epitopes. Scale bar = 20µm. All images were taken in the SN or transentorhinal cortex of patient PD2. Different IHC features are flagged (discussed in text). Black and white arrowheads highlight aSyn-immunopositive neuronal inclusions. In xviii, a weaker ring of immunopositivity (white dot) surround the portion with strongest labeling (indicated with a ^). In xxviii, a dystrophic LN is indicated by an asterix. **B:** Example of a dystrophic LN with with stronger immunolabeling at its periphery compared to its core, as observed using an antibody against Ser129-p aSyn (11A5) in the SN of patient PD4. Scale bar = 10µm.

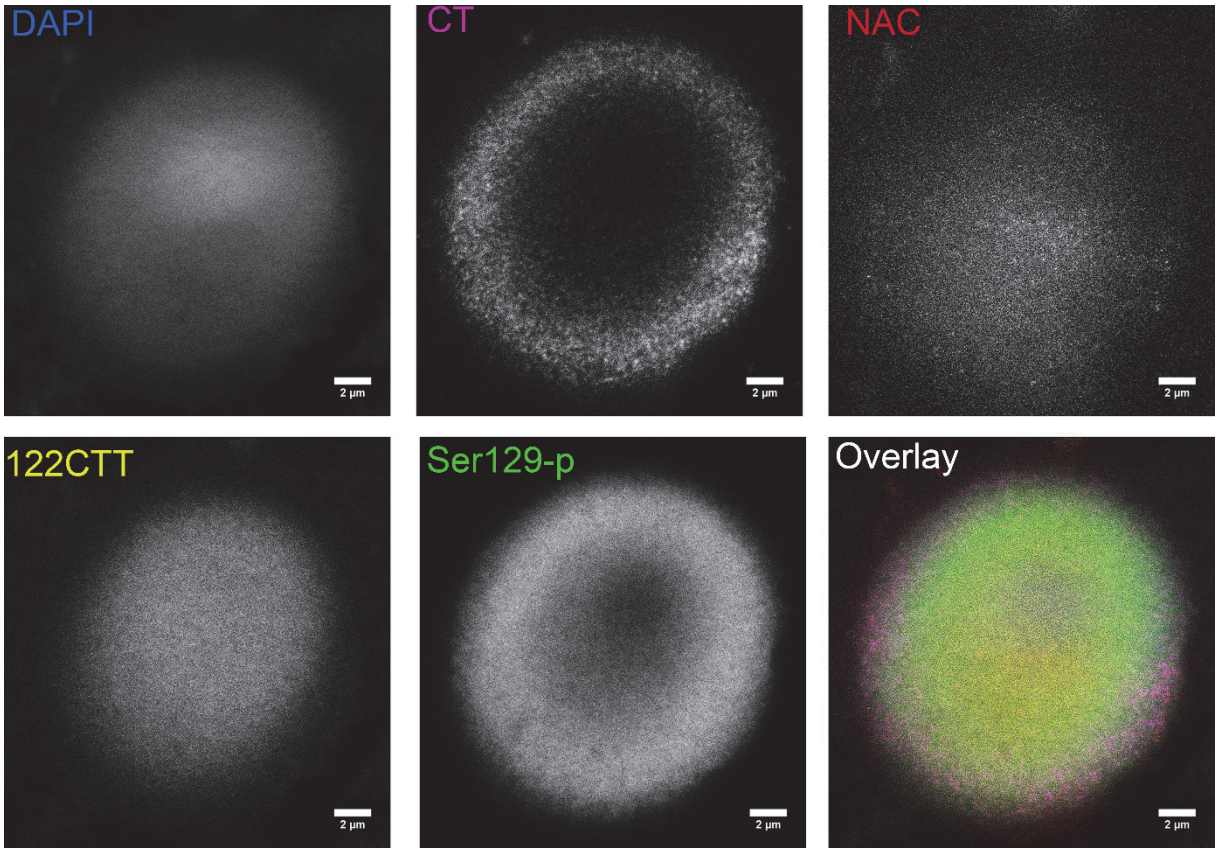

Figure S2: Multilamellar pattern of immunoreactivities for different aSyn epitopes in onion-skin like LBs is observed with different antibodies (validation set). Raw STED images taken in the SN of patient PD7. Scale bar: 2µm

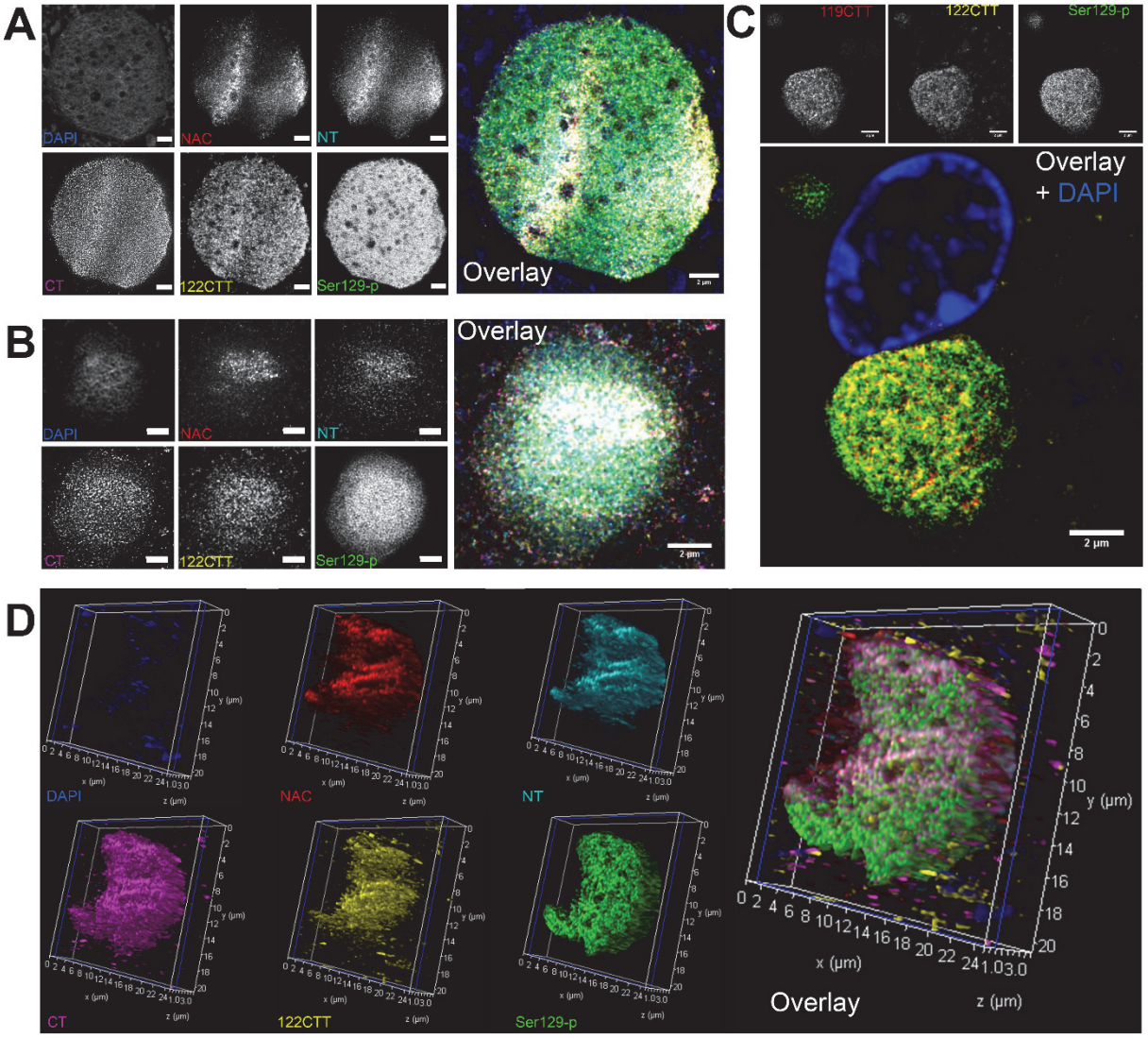

Fig S3: Diffuse distribution patterns of aSyn PTMs and domains in non-onion skin type aSyn inclusion body morphologies. A. B. C: Representative deconvolved STED images of inclusion bodies/LBs in the SN, transentorhinal cortex, and hippocampus of patient PD4. The distribution of immunoreactivities was generally diffuse, although CT and Ser129-p aSyn immunoreactivity at the edges of the structure often sharply delineated the inclusion. **D.** 3D reconstruction of a compact LB in the SN based on deconvolved CSLM images, taken in patient PD7. **A-C:** Scale bar = 2 µm

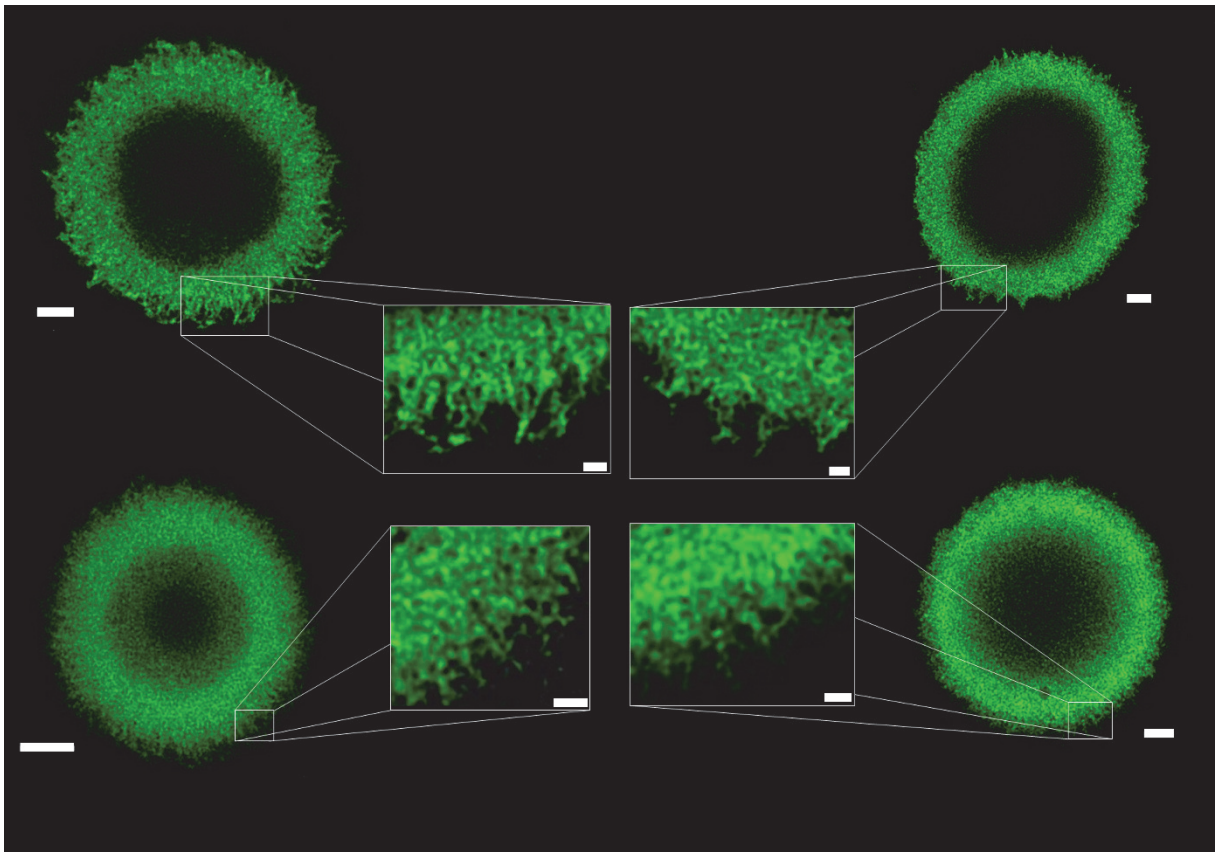

Figure S4: Gallery of radiating Ser129-p positive filamentous structures in nigral LBs. The outline of midbrain LBs often shows a corona of radiating Ser129-p aSyn immunoreactivity. STED deconvolved images taken in the SN of different PD patients. Scale bars main Figure = 2µm; scale bars insets = 0.5µm

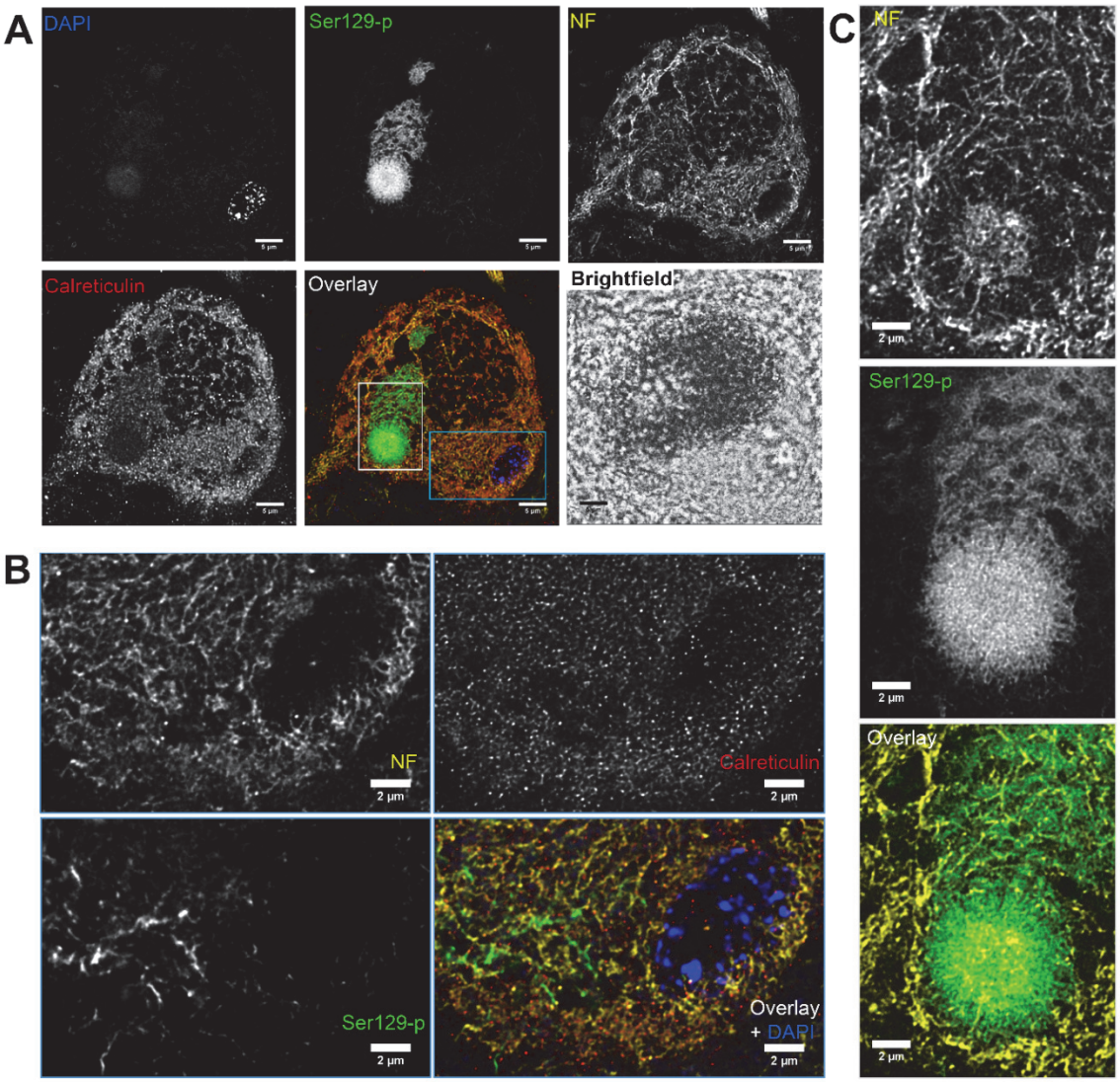

Figure S5: Intracytoplasmic 129Ser-p aSyn network shows limited co-localization with other intracytoplasmatic networks (part 2). Images were taken in a dopaminergic neuron the SN of a PD patient containing a combination of a combination of expansive-appearing inclusion and a small LB with a barely distinguishable ring-structure. **A:** Overview: deconvolved CSLM images of the entire neuron showing different intracytoplasmatic networks reactive for calreticulin (ER marker), neurofilamentand Ser129-p aSyn. Note the limited availability of epitope in the area containing neuromelanin (visible in brightfield image as dark material). **B:** Detailed view on the area in the blue square indicated in **A**. Deconvolved STED images showing limited co-localization between markers for intracytoplasmic networks of neurofilament. **C:** Detailed view of the inclusion (area indicated

in the grey square in **A**). The compact-appearing spherical LBs shows 1) radiating filaments immunopositive for Ser129-p aSyn; 2) a cage-like framework of neurofilament. NF: intermediate neurofilament.

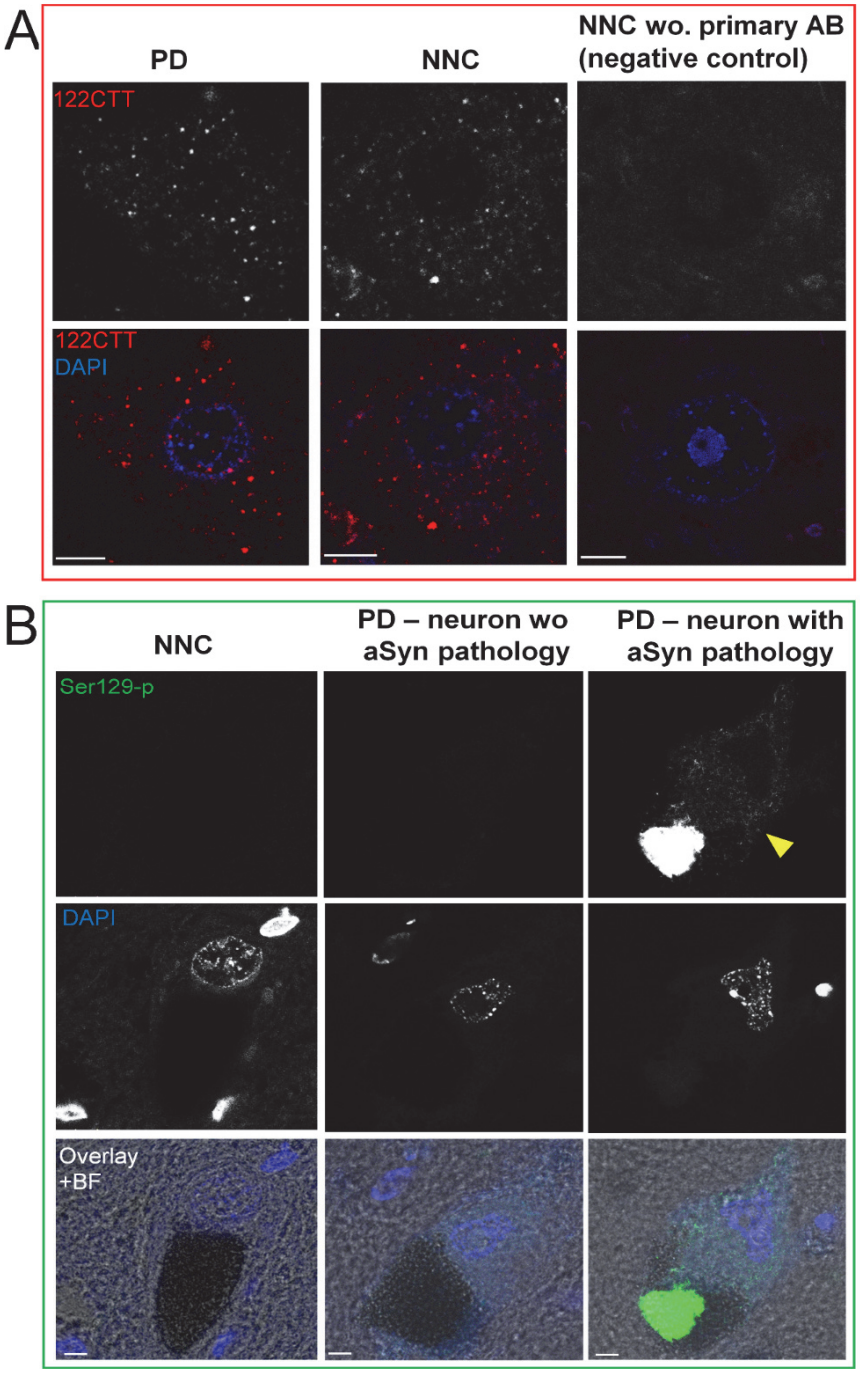

Figure S6: Subcellular reactivity patterns for CTT and Ser129-p aSyn in brains with and without Lewy pathology. A) The dot-like pattern of 122CTT aSyn was visible both in

PD patients and brains without Lewy pathology (NNC = non-neurological control). However this pattern was not observed in negative controls lacking the primary antibody. Images taken in the hippocampus, scale bar = 5µm. **B:** The cytoplasmic fibrous Ser129-p positive network (indicated by yellow arrowhead) was only observed in certain cells in PD patients – often associated with the presence of an inclusion - and not in non-demented controls. Raw CSLM images that were scanned, processed and visualized in the same way. Images taken in melanin-containing cells in the SN, scale bar = 5 µm. **Abbreviations:** NNC = non-neurological control; BF: brightfield

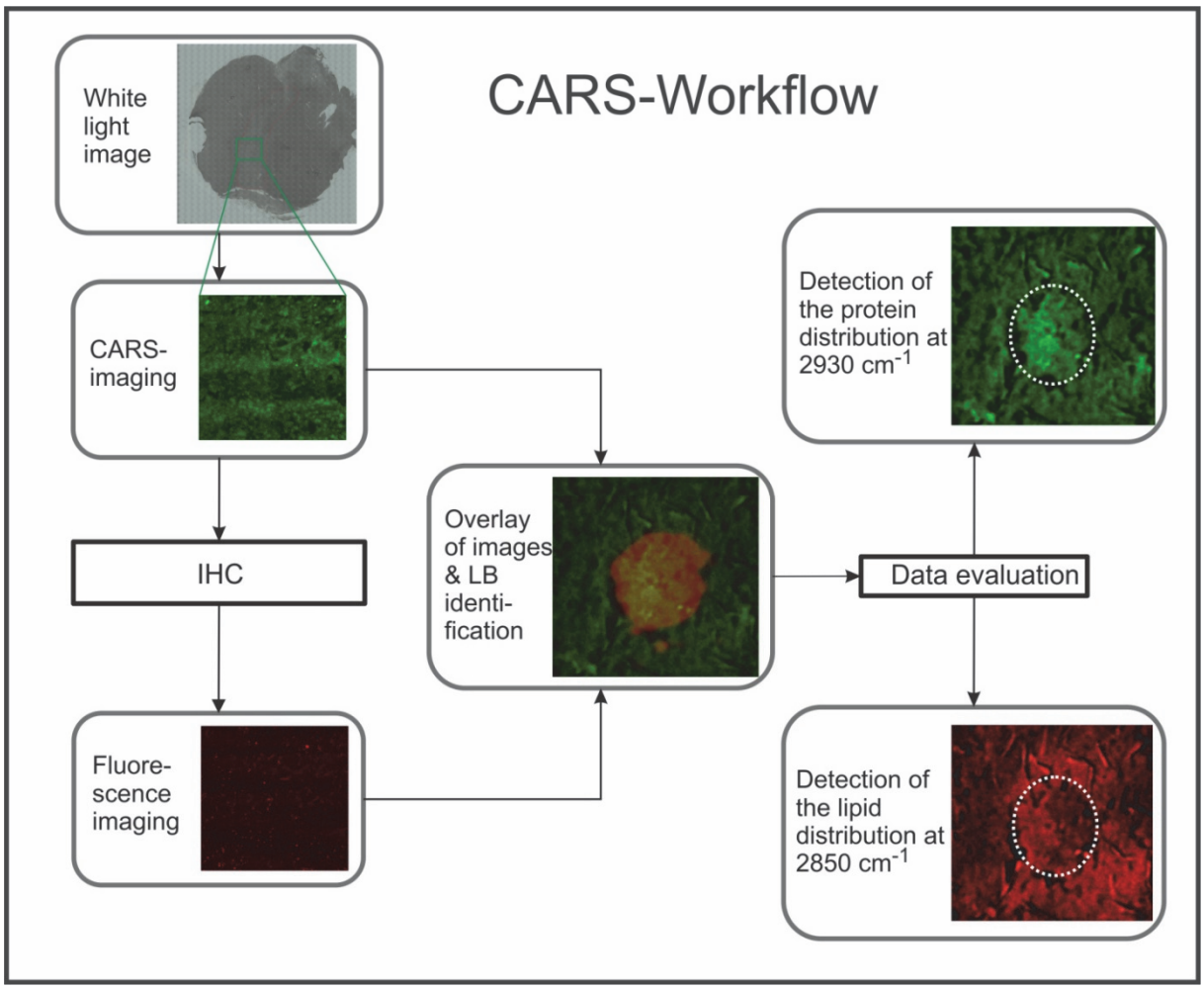

Figure S7: CARS-Workflow for the detection of the lipid and protein distribution in Lewy bodies. White light images were measured to detect the SN. The CARS-intensity was

measured as overview images. On the same slide an immunohistological staining was performed and the fluorescence was detected for aSyn and Ser129-p aSyn. The images were manually overlaid. LBs were identified and small regions-of-interest (ROIs) were extracted. These ROIs were evaluated and the protein and lipid distribution of aSyn-positive inclusions was detected.

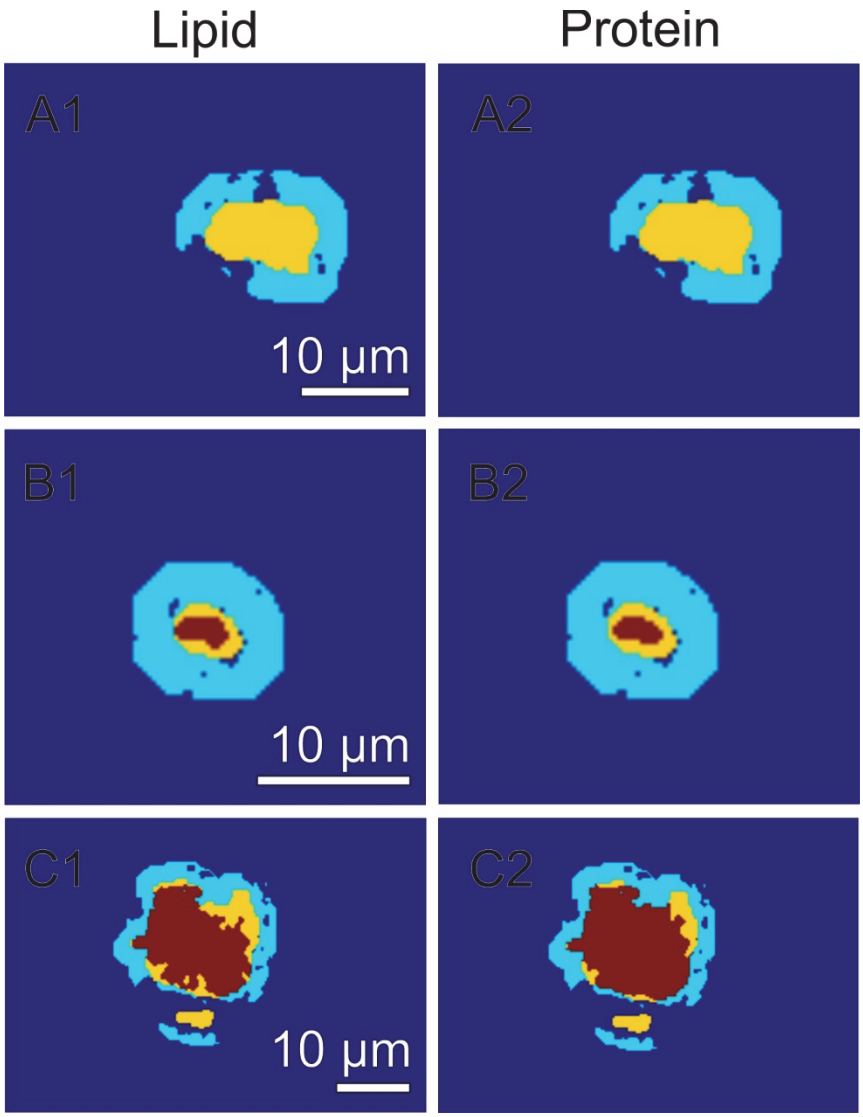

Figure S8: Evaluation of the centralization of lipids and proteins by CARS. The LBs were identified by aSyn staining (yellow) in the CARS-intensity images. For an objective

evaluation of CARS intensity of the LBs, the mean CARS intensity of the direct surrounding (A, cyan), a donut with a width of 3.5 µm, was compared with the CARS-intensity of each LB pixel (A, yellow). CARS-pixel-intensities higher than 1.4 times the mean CARS-intensity of the surrounding were defined as higher protein/lipid content. The ratio between the CARS-pixel-intensities of the LB and the mean CARS intensity of the surrounding were calculated and areas with higher protein/lipid content were marked in red. Areas without CARS intensity (holes) were excluded by intensity thresholding in the first step.

Legends for supplementary video files:

Video S1: 3D reconstruction based on deconvolved CSLM images revealing the distribution of Ser129-p. 119CTT and 122CTT aSyn in an onion-skin type LB in the SN of patient PD7.

Video S2: 3D reconstruction based on deconvolved CSLM images revealing the distribution of Ser129-p. 119CTT and 122CTT aSyn in another onion-skin type LB in the SN of another patient (PD6).

Video S3: 3D reconstruction based on deconvolved CSLM images revealing the distribution of antibodies directed against NT, NAC domain and CT in a onion-skin type LB in the SN of patient PD8.

Video S4: 3D reconstruction of an entire onion-skin type LB based on deconvolved CSLM images showing the distribution patterns of antibodies against different PTMs and domains of aSyn in the SN of patient PD1.

Video S5: 3D reconstruction based on deconvolved CSLM images of expansive-appearing inclusion body showing the distribution patterns of antibodies against different PTMs and domains of aSyn in the SN of patient PD8.

Video S6: 3D reconstruction based on deconvolved STED images showing the filamentous cage-like framework formed by Ser129-p aSyn and cytoskeletal components at the periphery of an onion-skin type LB in the SN of patient PD7.

Video S7: 3D reconstruction based on deconvolved STED images showing localization of a CTT-reactive punctae at the outer membrane of a mitochondrion immunopositive for VDAC/Porin in the hippocampus of patient PD4.